2P-NucTag: on-demand phototagging for molecular analysis of functionally identified cortical neurons

Authors: Jingcheng Shi[1,2,3,*], Boaz Nutkovich[5,6,*], Dahlia Kushinsky[5,6,*], Bovey Y. Rao[1,2,3,*], Stephanie A. Herrlinger[1,2,*], Emmanouil Tsivourakis[4,5,6], Tiberiu S. Mihaila[1,2], Margaret E. Conde Paredes[1,2,3,7], Katayun Cohen-Kashi Malina[5,6], Cliodhna K. O'Toole[1,2], Hyun Choong Yong[1,2], Brynn M. Sanner[1,2], Angel Xie[1,2], Erdem Varol[7], Attila Losonczy[1,2,#,‡], and Ivo Spiegel[5,6,#,‡]

Affiliations:
[1] Department of Neuroscience, Columbia University, New York, NY, United States
[2] Mortimer B. Zuckerman Mind Brain Behavior Institute, Columbia University, New York, NY, United States
[3] Doctoral Program in Neurobiology and Behavior, Columbia University, New York, NY, United States
[4] Stavros Niarchos Foundation Center for Precision Psychiatry and Mental Health, New York, NY, United States
[5] Department of Brain Sciences, Weizmann Institute of Science, Rehovot, Israel
[6] Department of Molecular Neuroscience, Weizmann Institute of Science, Rehovot, Israel
[7] Tandon School of Engineering, New York University, New York, NY, United States

[*] Co-first authors
[#] Co-senior authors
‡ Corresponding authors. Emails: al2856@columbia.edu, ivo.spiegel@weizmann.ac.il

Summary:
Neural circuits are characterized by genetically and functionally diverse cell types. A mechanistic understanding of circuit function is predicated on linking the genetic and physiological properties of individual neurons. However, it remains highly challenging to map the molecular properties onto functionally heterogeneous neuronal subtypes in mammalian cortical circuits *in vivo*. Here, we introduce a high-throughput two-photon nuclear phototagging (2P-NucTag) approach for on-demand and indelible labeling of single neurons via a photoactivatable red fluorescent protein following *in vivo* functional characterization in behaving mice. Using this novel function-forward pipeline to selectively label and transcriptionally profile previously inaccessible 'place' and 'silent' cells in the hippocampus of behaving mice, we identify unexpected differences in gene expression between these hippocampal pyramidal neurons with distinct spatial coding properties. Thus, 2P-NucTag opens a new way to uncover the molecular principles that govern the functional organization of neural circuits.

One-Sentence Summary: 2P-NucTag - A novel high-throughput on-demand phototagging approach to identify selective gene expression of functionally distinct neurons *in vivo* in behaving animals.

Introduction

Information processing in neural circuits requires precise interactions between molecularly and functionally diverse populations of neurons. Since gene expression dictates neuronal connectivity and function, a fundamental goal of neuroscience has been to characterize gene expression profiles of functionally defined neurons and to measure changes in gene expression associated with distinct functional states of neurons[1]. High-throughput transcriptomic approaches such as single-cell/-nucleus RNA-sequencing (sc/snRNA-seq) and spatial transcriptomics have greatly accelerated the identification of gene programs in molecularly distinct types of neurons at single-cell resolution[2–8]. However, functional and anatomical characterization of such molecularly identified neuronal subtypes[9–13] remains highly challenging as it requires the generation and validation of new subtype-specific molecular tools[14–16]. Recently, correlated *in vivo* Ca^{2+} imaging with *post hoc* spatial transcriptomics (ST) has been used to relate gene expression with *in vivo* function[17–20], but this approach is limited by the relatively low density of the cells investigated and by the number of genes that can be probed in ST experiments. Furthermore, this approach is not suitable for unbiased transcriptomic analyses as selecting probes for ST requires prior knowledge of the genes of interest. Therefore, a method for unbiased identification of genes that are differentially expressed in densely packed, functionally distinct glutamatergic pyramidal neurons (PNs) would significantly accelerate our understanding of how gene expression determines circuit function and behavior.

The inability to tag single functionally identified cortical PNs *in vivo* in behaving animals presents a significant challenge as large-scale neural recordings have shown that PNs are highly heterogeneous in their physiological, anatomical, and response properties, and are spatially intermixed within neocortical and hippocampal circuits[16,21–27]. For example, PNs with distinct spatial coding properties are distributed throughout the dense cell body layer of the hippocampus[28–35]. However, the origin of this functional diversity in feature selectivity is largely unknown, and it remains unclear if gene expression differences are associated with discrete and transient functional cell states[35–40]. Thus, there is a critical need for function-forward approaches to directly identify the transcriptional profiles of cortical neurons that were functionally characterized *in vivo* in behaving animals, and to test subsequently whether the functional differences between seemingly identical neurons are indeed driven by specific differentially expressed genes.

Previous attempts using Ca^{2+} and light-dependent labeling of transiently active neurons[16,41–43] were limited by their spatial resolution, deficiencies in targeting neurons with high baseline intracellular Ca^{2+} levels, and the inability to label neurons that decrease their activity in response to behavioral state or sensory stimuli. Similarly, labeling approaches based on the expression of immediate early genes [44–47] lack the temporal and spatial resolution to faithfully report the precise activity patterns and response properties of single neurons that are active but functionally distinct (e.g., neurons with different response tuning properties or feature selectivity). Finally, previous attempts to tag cortical neurons with photoactivatable fluorescent proteins[48] with single-cell precision have been deployed with limited success[49]. Thus, although these methods, collectively, have contributed greatly to the understanding of how co-active cells contribute to behavior and cognition, there is an unmet need for an approach that allows for identifying the molecular and cellular properties of single neurons that were functionally characterized *in vivo* based on their precise activity patterns in behaving animals.

Here we introduce 2P-NucTag, a robust *in vivo* pipeline for in-depth molecular and cellular analyses of single neurons that were functionally characterized in behaving animals. The 2P-

NucTag approach optimizes a previously described *ex vivo* framework[50] and is based on the co-expression of a photoactivatable red fluorescent protein (PAmCherry) and a genetically encoded green Ca^{2+} indicator (GCaMP7f or GCaMP8s) - thereby, 2P-NucTag allows for combining large-scale *in vivo* two-photon (2P) functional imaging of cortical PNs with reliable and selective 2P phototagging of the nuclei of single neurons based on their functional properties as well as with *post-hoc* in-depth unbiased transcriptomics and cellular analyses of the photolabeled neurons. Using this novel approach, we identify unexpected differences in gene expression and cellular properties in previously inaccessible 'place' and 'silent' cells in the hippocampus of behaving mice. Thus, we achieve previously unattainable molecular characterization of functionally identified PNs *in vivo* in behaving animals using the 2P-NucTag approach.

Results

In vivo two-photon phototagging with 2P-NucTag

A major challenge in combining *in vivo* functional recording with stable tagging in the same neuron is the co-expression of an activity sensor and a photoactivatable tag with spectrally separable fluorescent imaging and photoactivation. We overcame this challenge by generating a bicistronic construct on a recombinant adeno-associated viral (rAAV) backbone that co-expresses cytosolic GCaMP7f[51] for 2P Ca^{2+} imaging and a nucleus-targeted photoactivatable red fluorescent protein (H2B-PAmCherry) for 2P phototagging[50] via a promoter that is selective for cortical glutamatergic neurons[52] (2P-NucTag, Figure 1A). Upon injection of the 2P-NucTag rAAV into the CA1 region of the mouse dorsal hippocampus to label CA1 PNs, we found that GCaMP7f is properly expressed in the perinuclear space of the infected PNs (Figure 1B). Targeting the nuclei of GCaMP-expressing neurons, we achieved rapid nuclear PAmCherry photoconversion using 810-nm excitation light on a three-dimensional acousto-optical deflector microscope (3D-AOD)[53,54] (Figure 1B; supplementary movie 1, see methods) and orthogonal GCaMP-Ca^{2+} activity imaging with 940 nm excitation light (Figure S1A-B). Photoconverted PAmCherry red fluorescence was detected at >1000 nm excitation (1040 or 1070 nm, see Methods) and was localized to the targeted nuclei (Figure 1B, top). 2P-NucTag enabled the imprinting of arbitrary tagging patterns into the CA1 pyramidal cell layer with 3D-AOD scanning, showing spatially precise photoconversion of H2B-PAmCherry with single-nuclear and even sub-nuclear resolution (Figure 1B, middle and bottom). We carried out a detailed characterization of wavelength, laser power, and duration-dependence of PAmCherry photoactivation *in vivo* to identify the optimal parameters for spatially precise photoactivation (Figure 1C). Based on our results, we opted for 810 nm excitation light with 37-42 mW laser power (measured after the objective), 1.3 ms/pixel dwell time over 70 pixel x 70 pixel regions-of-interest (ROIs, with 0.1 μm/pixel resolution). The 810-nm wavelength is spectrally separated from the GCaMP-based Ca^{2+} imaging wavelength at 940 nm, and these photoactivation wavelengths, laser power, and duration parameters yielded robust increases in PAmCherry fluorescence of targeted nuclei (192-379% increase in PAmCherry red fluorescence visualized using 1040 nm excitation: n = 36 cells, 295% ± 8% $\Delta F/F$, mean ± s.e.m.) after single scans while minimizing total scan time and power. We confirmed that phototagged nuclei remained detectable over multiple days after photolabeling (Figure 1D). We next photoactivated a subset of CA1 PNs in a large (700 x 700 μm) field of view (FOV), similar to the FOV size used for *in vivo* 2P population imaging experiments in CA1 (Figure 1E, left). We found clear photoactivation of individual target nuclei when visualized *in vivo*. We then confirmed that *in vivo* photolabeling was preserved in *post hoc* histological slices (Figure 1E, middle), and

that phototagged cells can be reliably registered across *in vivo* z-stacks and *post hoc* confocal images (Figures 1E, right, 1F, S1C-D, supplementary movie 2). In addition, we segmented the nuclei from both the *in vivo* and *ex vivo* z-stacks to observe the average axial and lateral fluorescence profiles of phototagged nuclei, demonstrating single-nucleus resolution (Figure 1F, right).

To establish the compatibility of the 2P-NucTag construct with downstream cell sorting and transcriptomic applications, we further prepared CA1 PN samples and subjected them to FACS and Meso-seq (Figure S2). We chose to use our previously developed Meso-seq protocol due to its advantage of providing a robust and cost-effective method for sequencing low numbers of input nuclei. We collected 3 samples from AAV-transduced nuclei ('Injected, transduced'), 2 samples of nuclei that were not transduced but were isolated from the mice that received AAV injections ('Injected, non-transduced'), and 2 negative control samples from mice that were not injected with AAVs ('non-injected'). For each sample, 50-100 nuclei were collected and analyzed in bulk via Meso-seq. Between these groups, we found that they have comparable sequencing statistics in terms of total reads and percent of uniquely mapped reads (Figure S2A); notably, these sequencing statistics were similar to those when we applied Meso-seq to AAV-infected visual cortex samples in previous studies[55,56]. Gene expression levels between groups were highly correlated (Figure S2B-C) and reads of representative genes were similar between groups except for the inhibitory neuron markers (Figure S2D). Thus, our results demonstrate that the previously established Meso-seq protocol works well with low numbers of hippocampal PN nuclei as input, and that the 2P-NucTag construct does not cause changes in transcriptional properties in AAV-infected PNs. We also obtained *ex vivo* whole-cell patch-clamp intracellular recordings from phototagged and control CA1 PNs (Figure S3A) in acute hippocampal slices: comparing H2B-TAG (infected and photoactivated), H2B (infected), and control (non-infected) cells revealed no differences in intrinsic properties (Figure S3B-G). Together, these results confirm the utility of 2P-NucTag to analyze *ex vivo* the cellular properties of single CA1 PNs that were functionally characterized and phototagged *in vivo* and demonstrate that the 2P-NucTag construct does not affect the intrinsic physiological properties of these PNs. Thus, 2P-NucTag enables high-throughput, indelible phototagging of neuronal nuclei *in vivo* that can also be identified via our registration pipeline for *post hoc* analyses *ex vivo*. Phototagged nuclei further enable downstream RNA-sequencing and *ex vivo* electrophysiology analyses.

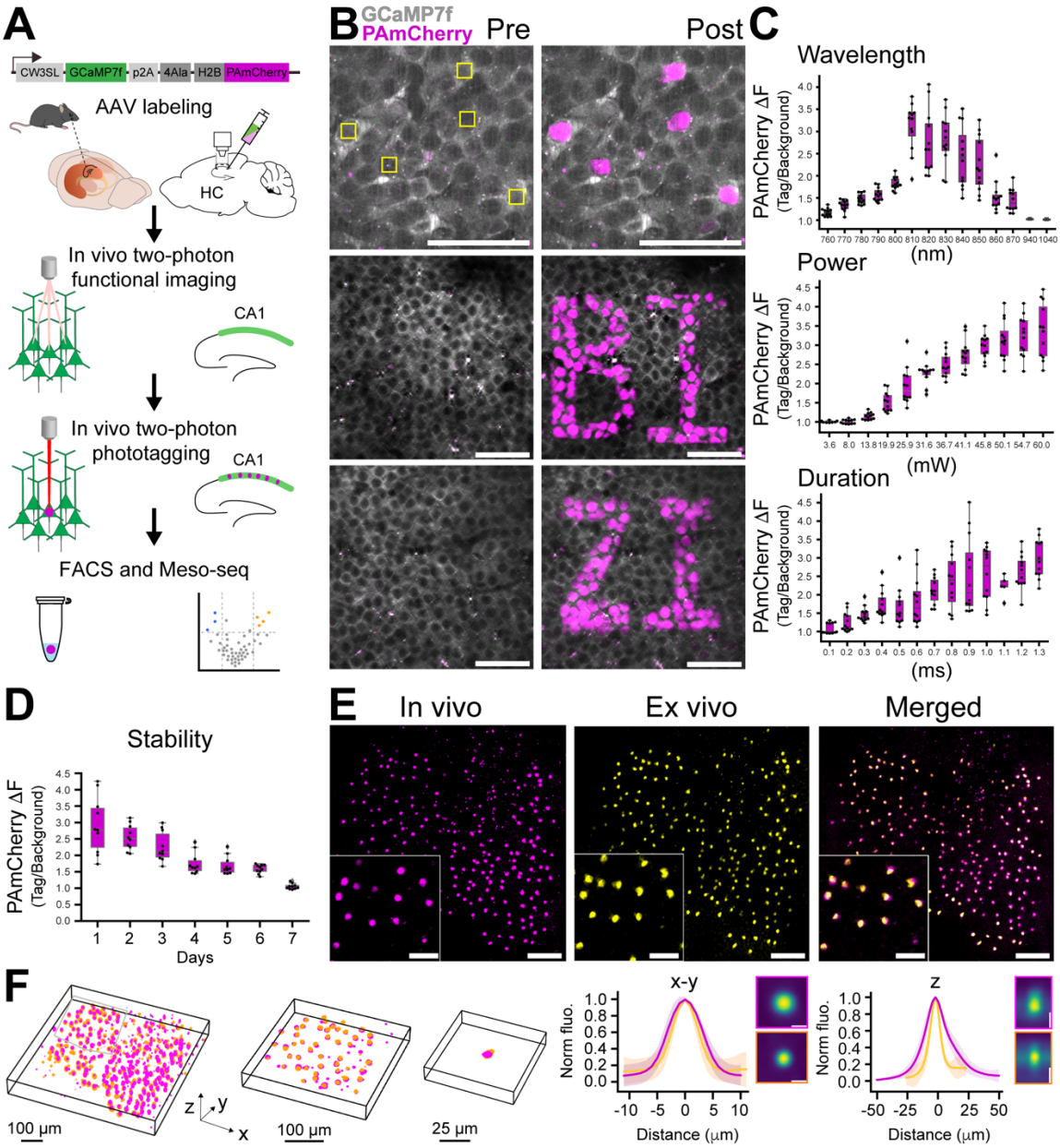

Figure 1. *In vivo* two-photon phototagging with 2P-NucTag. (**A**) Schematics of the 2P-NucTag pipeline. Top: bicistronic rAAV construct, injection to the hippocampus. Middle: *in vivo* two-photon (2P) GCaMP- Ca^{2+} population imaging followed by 2P PAmCherry photoactivation, fluorescence-activated cell sorting (*FACS*), and mesoscale sequencing (*Meso-seq*). (**B**) Top: representative *in vivo* time-averaged (6 frames average) 2P images of individual cells before (*Pre*) and after (*Post*) *in vivo* two-photon PAmCherry photoactivation in the CA1 pyramidal layer of the mouse dorsal hippocampus. Individual nuclei were photoactivated with 810-nm 2P laser chessboard scanning region-of-interest (ROI, yellow boxes) over target nuclei (70 x 70 pixel for each ROI, 0.1 µm/px, 1.3 ms/px total pixel dwell time, 6,370 ms total scan time per ROI. Laser power was 40 mW measured after the objective) with a 3-dimensional acousto-optical deflector microscope (3D-AOD). Gray: GCaMP7f (940 nm excitation), magenta: PAmCherry, (1040 nm excitation). Scale bar: 50 µm. Middle and bottom: imprints of letters '*BI*' and *'ZI'* following patterned *in vivo* two-photon photoactivation in the hippocampal CA1 pyramidal layer (scale bar, 50 µm). (**C**) Characterization of *in vivo* 2P photoactivation parameters for PAmCherry: duration, wavelength, laser power (measured after the objective) (n = 11-12 cells per condition). Relative change in PAmCherry red fluorescence (ΔF) is based on normalizing the tagged nuclei fluorescence to the fluorescence of neighboring untagged nuclei measured with 1040 nm excitation. **(D)** *In vivo* stability of the PAmCherry fluorescence signal over days after a single photoactivation scan (n = 8 cells). (**E**)

Representative time-averaged images from z-stacks of photoactivated nuclei *in vivo* (magenta: PAmCherry, scale bar: 100 μm). Middle: *ex vivo post hoc* confocal z-stack image of the same field of view (FOV, magenta: PAmCherry). Right: registered *in vivo* and *ex vivo* images following non-rigid image transformation (magenta: *in vivo*, yellow: *ex vivo*, see methods). (**F**) Left: 3D overlay of tagged nuclei registered between *in vivo* (magenta) and *ex vivo* (yellow) z-stacks with increasing lateral resolution (as in *E*). Gray box represents the segmented area for subsequent images. Right: normalized lateral (*x-y*, left) and axial (*z*, right) fluorescence profiles (mean ± s.e.m.) of tagged cells *in vivo* (magenta, n = 1 mouse, 200 cells). Yellow: mean ± s.e.m. of *ex vivo* confocal images (as in *E* and *F,* same mouse and nuclei). Inset: (x-y) top: average *in vivo* maximum z–projection, bottom: average *ex vivo* maximum z projection; (z) top: average *in vivo* lateral projection, bottom: average *ex vivo* lateral projection. Scale bar: 10 μm. Boxplots show the 25th, 50th (median), and 75th quartile ranges, with the whiskers extending to 1.5 interquartile ranges below or above the 25th or 75th quartiles, respectively. Outliers are defined as values extending beyond the whisker ranges.

Phototagging of functionally identified PNs in the hippocampus *in vivo*

To demonstrate the utility of 2P-NucTag for on-demand labeling of functionally defined PNs, we deployed 2P-NucTag to label hippocampal PNs located in the dorsal CA1, a region with well-established spatial coding heterogeneity[28–35]. Only a subset of hippocampal PNs ('place cells') exhibit reliable spatial tuning for a location ('place field') during exploration[57]. Place cell identity of PNs[58] is highly dynamic, with the majority of cells changing their spatial tuning properties over the timescale of days[35–40]. While place cell properties of PNs were thought to be randomly allocated onto seemingly homogeneous PNs[58], recent studies demonstrated that the genetic expression profiles of CA1 PNs are also highly heterogeneous[30,32,59]. These transcriptional differences are present along all anatomical axes of the hippocampus[29], manifest at the protein expression level, and are comprised of genes with known functions (e.g., transcription factors, cell adhesion molecules, voltage-gated channels, neurotransmitter receptors, and auxiliary subunits)[29,60]. Gene expression differences thus could produce variability in the biophysical properties and connectivity of PNs and may underlie the differences in stable spatial coding properties of CA1 PN subpopulations. Thus, the spatial intermingling of place cells with active-non-place and silent PNs[61–64] without apparent topographical organization in the densely packed CA1 pyramidal layer[35,64] allows us to test the utility of 2P-NucTag in selectively labeling PNs occupying these distinct functional states.

To selectively label CA1 PNs with distinct spatial coding properties, we trained mice in a spatial navigation task for water rewards in a linear virtual reality environment[65–67] and performed *in vivo* 2P GCaMP- Ca^{2+} imaging of PNs (Figure 2A-B). We reliably detected GCaMP-Ca^{2+} signals from individual PNs (Figures 2C, S1B). We analyzed the basic characteristics of GCaMP7f in the bicistronic 2P-NucTag construct and confirmed that the basic properties of the indicator are similar to those for a previously published single-construct version[51] of GCaMP7f (Figure S1B). We classified all PNs in the imaging FOV as place cells, active non-place cells, or silent cells (Figure 2D, see methods). Place cells were identified as described in our previous studies[38,67–69] where place fields were detected by identifying spatial tuning curves surpassing the 95th percentile of shuffled tuning curve values, and silent cells were classified as cells with no deconvolved events in the recording session. Following the functional identification of PNs, we generated spatial masks of place cell locations in the FOV and used these masks to guide 2P phototagging of all identified place cells in the imaging FOV with 3D-AOD (n = 5 mice, Figure 2E-F). In a separate set of mice (n = 4 mice), we tagged a subset of CA1 PNs that exhibited no detectable activity during the imaging session ('silent cells' see methods, Figure S4, Table 1), whereby we photoactivated a similar number of silent cells as place cells in each mouse despite their higher abundance in our recordings. We could reliably register photoactivated nuclei to the spatial masks of functional profiles that we generated for cells of interest (Figures 2F, S4D-E, S5, see methods).

188 We quantified the number of place cell nuclei that we successfully photoactivated and compared
189 it to the number of spatial masks we generated for each animal. For silent cells, we performed a
190 similar calculation with number-matched silent cell nuclei. Across all animals, we phototagged
191 93.3% ± 4.2% (n = 5 mice) of all place cell masks and 53.6 ± 6.6% (n = 4 mice) of all silent cells
192 (Figure 2F).
193 To assess the accuracy of 2P photoactivation in the densely packed CA1 pyramidal layer,
194 we quantified the number of tagged nuclei for each targeted cell and found that photoactivation is
195 well restricted to the target cells' nuclei with limited off-target labeled nuclei, which had a smaller
196 increase in mCherry fluorescence (Figures 2G, S4F). After tagging, mCherry fluorescence
197 increased in targeted place cells (487.7% ± 67% ΔF/F, n = 5 mice) more than double compared to
198 the background and off-target fluorescence (210.4% ± 32.1% ΔF/F, n = 5 mice). Furthermore, 2P
199 GCaMP-Ca^{2+} imaging at 940 nm over the course of the imaging session (18-40 min, see Methods)
200 resulted in a minimal increase of mCherry red fluorescence (37.4% ± 16.2% ΔF/F, n = 5 mice,
201 Figure 2G, right, Figure S4F, 1070 nm excitation) and did not affect our ability to identify
202 phototagged neurons. Finally, mouse behavior and the quality of GCaMP recordings were
203 consistent between the two groups of mice (silent and place, Figure S4G-I).
204 To further confirm that photoactivation of the PAmCherry does not change the functional
205 response properties of neurons, we expressed the 2P-NucTag construct in the primary visual cortex
206 (V1) of adult mice and recorded visually evoked responses of neurons in this region before and
207 after photoactivation (Figure S6A). We found that the orientation tuning (including both
208 preference and selectivity) remained largely the same in visually responsive neurons following
209 photoactivation (Figure S6B-C), indicating that activation of the PAmCherry does not alter
210 neuronal response properties. These experiments were conducted in the visual cortex due to the
211 known stability of its tuning properties[70].
212 Thus, taken together, our experiments demonstrate that 2P-NucTag is suitable for on-
213 demand *in vivo* labeling of functionally defined neurons with high efficacy and accuracy.

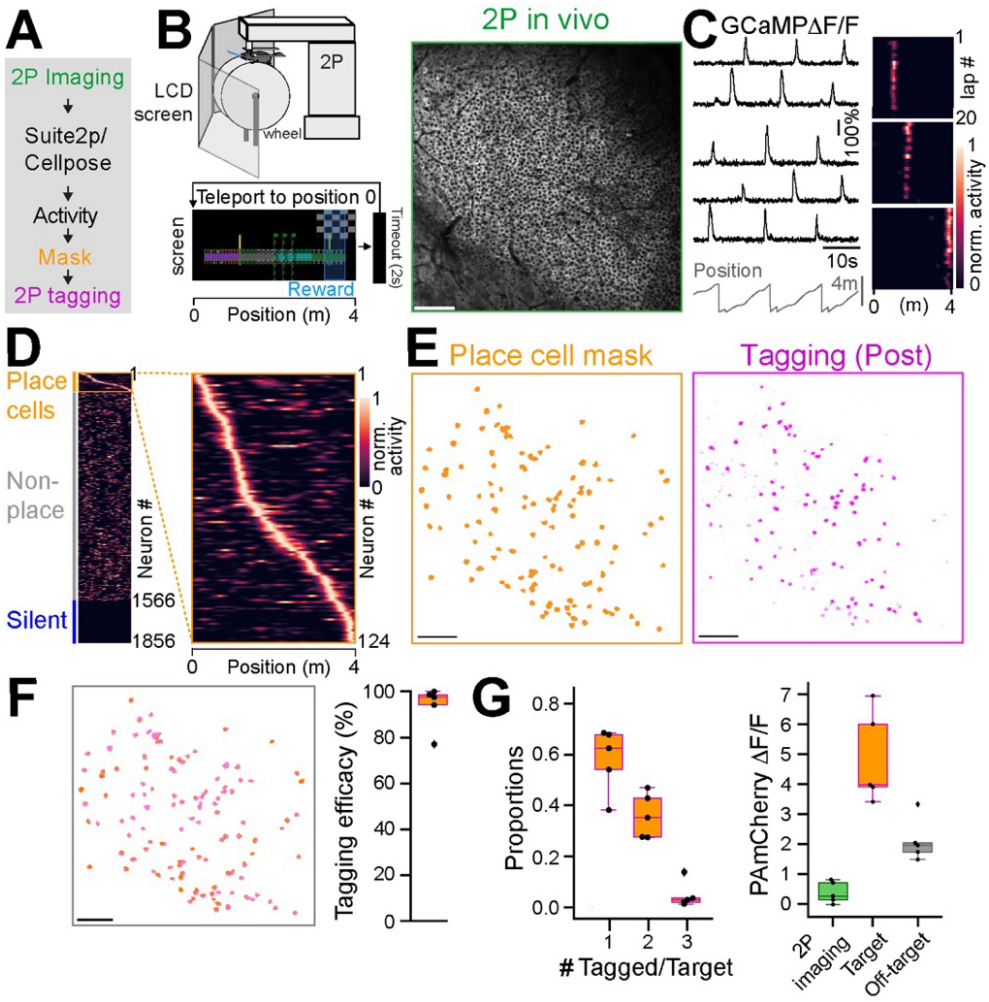

Figure 2. Selective phototagging of place cells in the hippocampus with 2P-NucTag. (**A**) Pipeline for two-photon (*2P*) phototagging of functionally identified hippocampal neurons during spatial navigation. (**B**) Left: schematics of 2P imaging setup in virtual reality (VR). Head-fixed mice are trained to run for a water reward in a 4-m long linear VR corridor projected onto LCD screens surrounding the animal. At the end of the corridor, mice are teleported back to the start position after a 2-second delay. Right: example 2P field of view (FOV) of GcaMP in the CA1 pyramidal layer. Scale bar: 100 µm.(**C**) Left: Traces of relative GcaMP-Ca^{2+} fluorescence changes (ΔF/F) from five example CA1 place cells during VR spatial navigation. Right: heatmaps of normalized ΔF/F activity from three example place cells over 20 laps during VR navigation. (**D**) Left: heatmap of all CA1PNs detected with Suite2p/Cellpose in the FOV shown in *B*. Identified place cells are marked with an orange box. Right: Zoomed-in heatmap of place cell tuning curves. (**E**) Left: spatial mask (orange) of identified place cells from *D* in the FOV. Right: PAmCherry fluorescence (magenta) of tagged nuclei after 2P phototagging. Scale bar: 100 µm. (**F**) Left: overlay of spatial masks of identified CA1PNs and tagged nuclei for the FOVs in *E*. Scale bar: 100 µm. Right: tagging efficacy, defined as the fraction of successfully tagged place cell nuclei (93.3% ± 4.2%, mean ± s.e.m., n = 5 mice). (**G**) Left: Proportion of single, double, and triple-tagged nuclei following phototagging of a single place cell. Right: relative change in PAmCherry red fluorescence (1070 nm excitation) for non-tagged cells in the FOV after 2P imaging (green), after 2P phototagging of targeted place cell nuclei (orange) and off-target nuclei (gray, n = 5 mice). Boxplots show the 25th, 50th (median), and 75th quartile ranges, with the whiskers extending to 1.5 interquartile ranges below or above the 25th or 75th quartiles, respectively. Outliers are defined as values extending beyond the whisker ranges.

Transcriptional profiling of functionally identified CA1 PNs

The ability to tag single cells *in vivo* enables a powerful new form of hypothesis generation and testing by which functionally defined cells with known behavioral relevance can be isolated and characterized. To demonstrate this, we sought to interrogate transcriptomic signatures of the functional 'place' and 'silent' cell states of CA1 PN.

Following functional imaging and *in vivo* phototagging, brain tissue containing dorsal CA1 was collected at least 25 hours after functional imaging to eliminate the impact of immediate early genes, and nuclei were dissociated and stained with a CoraLite 488-conjugated NeuN antibody and DAPI to identify neuronal nuclei (see Methods). *In vivo* photoactivated nuclei were identified by bright mCherry fluorescence (Figure 3A,B) and were isolated from the non-photolabeled neuronal nuclei by fluorescent-activated cell sorting (FACS), enabling an estimated 18-67% recovery of all photoactivated nuclei identified during in vivo imaging (Figure 3C). To validate that the FACS events with bright mCherry fluorescence were indeed the desired nuclei, we also performed sorting on samples derived from mice that were injected but not imaged; injected and imaged; or injected, imaged, and phototagged (Figure S7): we set the gates for mCherry fluorescence based on these samples and demonstrated that low mCherry fluorescence was induced by the imaging laser (Figure S7B) since the phototagged nuclei exhibited clearly identifiable higher mCherry fluorescence as compared to either of the other samples (Figure S7C). We then collected these bright nuclei collected for downstream transcriptomic analyses. To determine whether place cells and silent cells differed in their gene expression programs, RNA-seq was performed on both populations of sorted nuclei by Meso-seq, an approach that enables reliable identification of differentially expressed genes in ultra-low amounts for FACS-isolated neuronal nuclei (i.e., tens of sorted nuclei per animal, Figure 3D)[55]. After isolating the phototagged nuclei, libraries were generated with the Meso-seq protocol and were sequenced at a depth of 40-60 million reads per library (Figure S8A). Reads were aligned to the mm39 mouse genome assembly with STAR, counted with HTSeq, and gene expression patterns were compared between nuclei isolated from mice in which place cells were tagged (n = 5) and mice in which silent cells were tagged (n = 4) via PyDESeq2.

In both populations, canonical CA1 PN marker genes (*Map2, Actb, Dlg4, Neurod6*) were highly and non-differentially expressed, supporting the cellular precision of our tagging approach (Figure 3E-F). However, 219 genes were identified as differentially expressed in a significant manner between silent and place cells (Figure 3E, see Supplementary Table). In some cases, specific genes were reliably identified in one group and absent from the other. For example, no counts were measured for an inward rectifying potassium channel (*Kcnj12*) in place cell samples, but the expression was present in all silent cell samples. Conversely, mRNA from two transcription factors of the zinc finger protein family (*Zfp84, Zfp977*) and a protocadherin gene (*Pcdha8*) were identified in every place cell sample and in none of the silent cell samples (Figure 3G). To ensure that the observed differences did not arise from other sources of variation between our place and silent cell samples, we performed several additional analyses, investigating potential contributions from anatomical positioning, transcriptional responses to neural activity, cellular health, and sex. Genes for which expression has been shown to vary along the dorsoventral and proximodistal axes of CA1 were not differentially expressed in our place and silent-cell nuclei (Figure S8B)[29,71], indicating that any observed differences are unlikely to have originated from differences in anatomical positioning during cell tagging. Immediate early gene levels (*Fos, Arc, Egr1, Npas4*) did not differ (Figure 3F)[72–74], suggesting that the ≥25 hours between the last behavior session and tissue collection (see Methods) was sufficient time to eliminate the impact of immediate

transcriptional responses to neural activity. Apoptotic gene counts also did not differ between the two groups (Figure S8), indicating that there was no significant difference in cell health between the silent and place cells[75]. Finally, to test for gross molecular differences between the cells in an unbiased fashion, we performed gene set enrichment analysis on fifty hallmark gene sets from the mouse molecular signatures database and found no significant differences between silent and place cell samples (Figure 3H). Since the sex of mice used for both groups was not well balanced in this study (Table 1), it is possible that gene expression differences originated from the mouse's sex rather than the functional identity of the tagged cells. To explore this possibility, we compared gene expression in randomly tagged (function-blind) CA1 PN nuclei from both male (n = 2) and female (n = 2) mice. Although we found that known sex-specific genes[76] were differentially expressed, none of the genes identified as enriched in either silent or place cells had significant sex associations (Figure S9C,D). To assess if our differentially expressed genes-of-interest signified upregulation or downregulation in place cells from the mean or, conversely, downregulation or upregulation in silent cells, we compared gene expression in place cells and silent cells to randomly tagged cells separately. We found that *Kcnj12* expression was enriched in silent cells compared to random cells. *Zfp84* and *Zfp977* were significantly downregulated in silent cells compared to random cells, while *Pcdha8* expression was significantly enriched in place cells compared to random cells (Figure S9A,B).

Encouraged by our success in establishing 2P-NucTag for in-depth transcriptomic analyses in 'place' and 'silent' cells, we next sought to further develop this approach for additional key neurobiological applications. Specifically, we sought to test whether (1) the transcriptomic data obtained with the 2P-NucTag can be validated and used for dissecting the molecular mechanisms that determine functional properties of the phototagged neurons, and (2) 2P-NucTag can be used for more nuanced cell populations and resolve genetic changes of the same functional cell group at different timepoints.

For in-depth validation and functional analyses, we focused on *Kcnj12,* which our 2P-NucTag based transcriptomic analyses identified as expressed in silent cells but not in place cells. Since this gene encodes for an inward rectifying potassium channel Kir2.2[77–79], we hypothesized that its expression could reduce the intrinsic excitability of the neurons and make them more likely to be silent. Thus, we first validated the differential expression of *Kcnj12* by performing RNAScope Fluorescent in situ hybridization (FISH) in brain sections with tagged silent CA1 PNs (Figure S10). Using a probe set for detecting *Kcnj12* (Figure S10A), we quantified the number of *Kcnj12* puncta in tagged silent cells and a number-matched subset of randomly selected non-tagged cells (n = 247 cells each, n = 3 mice). These analyses confirmed that tagged silent cells indeed express more *Kcnj12* transcripts than non-tagged cells (Figure S10B). Similar RNAscope FISH experiments for *Pcdha8* (Figure S10C) further confirmed the specificity of our 2P-NucTag-based transcriptomic analyses since *Pcdha8* expression was enriched in tagged place cells as compared to randomly selected non-tagged cells (Figure S10D, n = 321 cells in each subgroup, n = 3 mice).

Next, we tested whether silent CA1 PNs differ in their intrinsic electrophysiological properties. For this, we performed targeted whole-cell patch-clamp recordings from tagged silent and nontagged cells *ex vivo* in acute hippocampal slices (Figure S11). Consistent with our hypothesis, we found that silent cells had a hyperpolarized resting membrane potential as compared to random non-tagged cells (Figure S11A). These experiments demonstrate the utility of the 2P-NucTag approach not only for molecular and analyses in functionally defined neurons but for connect *ex vivo* electrophysiological and cellular analyses of such *in vivo* labelled neurons.

Finally, to test whether the expression of Kir2.2 affects the likelihood of CA1 PNs to become place cells, we designed an AAV vector for Cre-dependent expression of Kir2.2 along with fluorescent protein mRuby3 (pAAV-hSyn-FLEX-Kir2.2$_{WT}$-T2A-mRuby3, Figure S12E); as a negative control, we also designed a vector that drives expression of an inactive (non-conducting) mutant of Kir2.2 (pAAV-hSyn-FLEX-Kir2.2$_{Mut}$-T2A-mRuby3, Figure S12E). We first co-injected these vectors along with an AAV to drive the expression Cre-recombinase (pAAV-hSyn-Cre) into the hippocampus of wild-type mice and assessed how ectopic expression of Kir2.2 affects the excitability of infected neurons. Using targeted whole-cell patch clamping, we found reduced excitability in cells expressing Kir2.2$_{WT}$ (Figure S12A-D) as these cells had lower resting membrane potentials, lower input resistance and lower firing rates across current steps when compared to cells with the control virus (Figure S12B-D). We then sought to test the effect of ectopic Kir2.2 expression on functional properties of CA1 PNs *in vivo* in behaving animals. We used two sets of mice in which we co-injected either of the Kir2.2 vectors along with AAVs for neuronal expression of GCaMP8s (pAAV-hSyn-GCaMP8s) and Cre-recombinase (pAAV-hSyn-Cre) and trained mice in the same behavior paradigm as described in Figure 2. We found that the cells expressing Kir2.2$_{WT}$ are more silent than mRuby3-negative cells in the same field of view, while these effects were not observed in cells with Kir2.2$_{Mut}$ (Figure S12F). Comparisons of spike rate and place cell percentage further indicated a silencing of activity and a lower proportion of place cells in Kir2.2$_{WT}$-expressing CA1 PNs (Figure S12G-H). Therefore, expression of Kir2.2 in CA1 PNs silences neurons, thereby affecting their *in vivo* function.

To further assess whether the 2P-NucTag approach can be used for molecular analyses in cells with even more nuanced differences in *in vivo* activity and function, we transcriptomically profiled place cells at different time points since a subset of these cells stabilizes their spatial representations over time and thus might differ in gene expression from when place cells first emerge. For this, we co-injected a version of 2P-NucTag AAV (pAAV-Ef1a-H2B-PAmCherry) with an AAV for pan-neuronal expression of GCaMP8s (pAAV-hSyn-GCaMP8s) into the hippocampal CA1 of two sets of mice. The mice were subsequently trained in a blank featureless environment and then recorded in a feature-rich environment (Figure S13A). In one group, we photo-tagged and collected place cells from day 0 of recording ('Day 0' cells), while in the other group we continuously recorded the same FOV for 5 days, and photo-tagged and collected place cells with at least 4 place fields across the 5 days of recording ('Recurring' cells, Figure S13B-C). Transcriptomic analyses were done with Meso-seq as described before. Using this approach, we identified 6 genes that were differently expressed (Figure S13D-F), including *Prkcd* and *Adamts1,* two genes enriched in 'Recurring cells' which were previously found to play a role in memory and synaptic connectivity[80,81] and which therefore might control the synaptic wiring of neurons to maintain long-term representation. Thus, we conclude that 2P-NucTag is useful for molecular analyses in more nuanced cell types and cells with the same functional identity at different timepoints.

Taken together, our results demonstrate that the 2P-NucTag approach allows for identifying the molecular and cellular properties of neurons in the same brain region that differ only by their activity patterns *in vivo* in behaving animals. Using this approach, we identify previously unappreciated transcriptomic differences in "place" and "silent" cells in the hippocampus of behaving mice and correlate these molecular profiles with the distinct electrophysiological properties of these cells. We further revealed that these differentially expressed genes affect the function of the respective groups of neurons by validating and demonstrating the role of *Kcnj12* in the excitability of CA1 PNs and the functional consequences

370 when ectopically expressed. The 2P-NucTag approach has the advantage of revealing previously
371 unknown molecular profiles of PNs and works with other methods to dissect the contribution of
372 specific molecular processes.

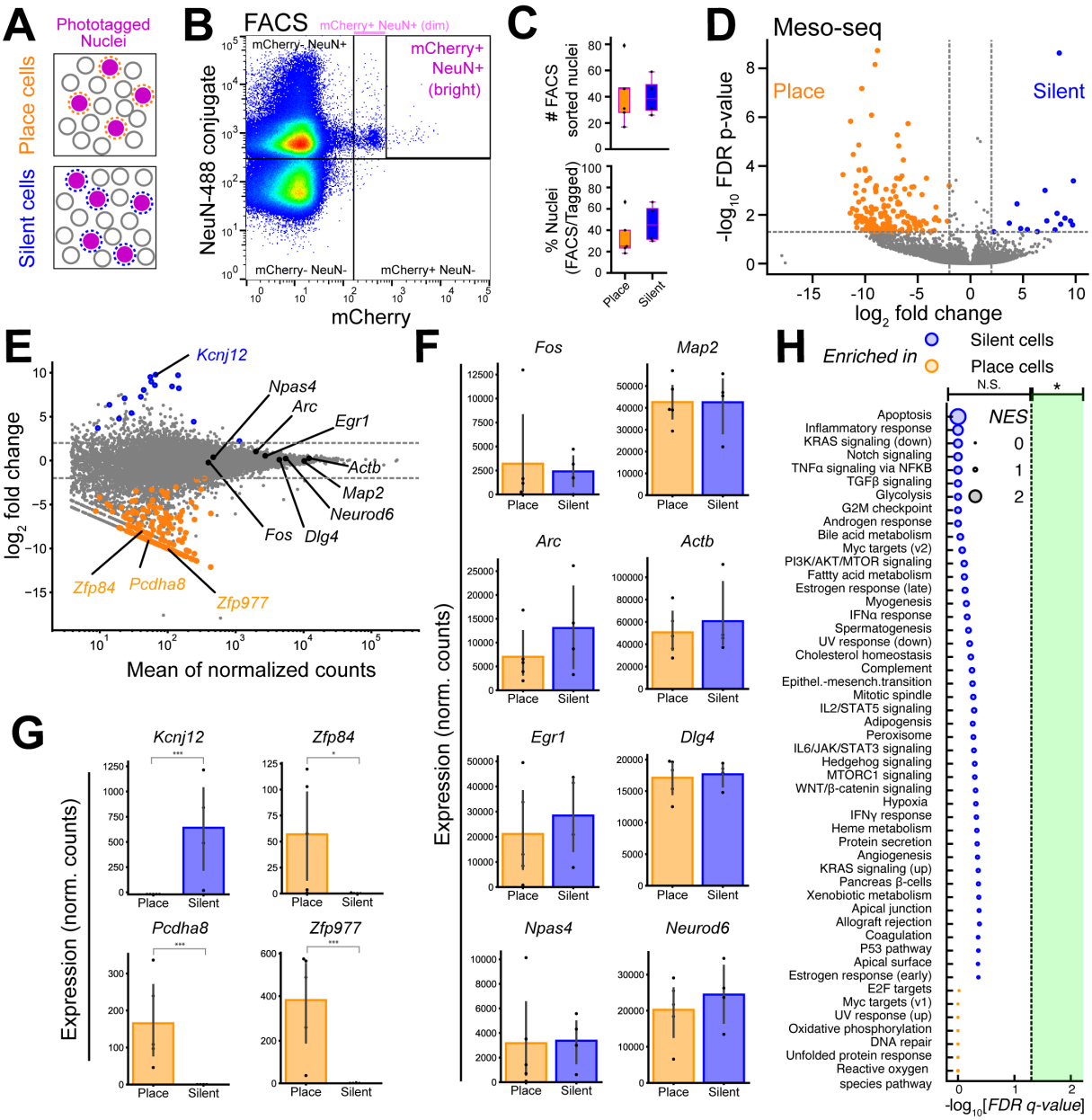

Figure 3. *Post hoc* transcriptional profiling of phototagged place and silent cells. (**A**) Schematics of *in vivo* photoactivated nuclei. 'Place' cell sample and 'Silent' cell samples from different mice were collected for FACS and Meso-seq. (**B**) Representative FACS graph. Gating for mCherry was set after the first 5000 events of DAPI+ nuclei to the border of the 'dim' mCherry+ population to separate out the sparse and high-intensity mCherry+ population. Bright mCherry+ NeuN+ populations were collected as the photoactivated nuclei. (**C**) Top: number of FACS sorted nuclei from 'place' and 'silent' samples (n = 9, 17-79 sorted nuclei, 40.3 ± 6.43, mean ± s.e.m.). Bottom: Proportion of FACS sorted nuclei compared to the number of *in vivo* photoactivated nuclei (n = 9, 18.45% to 66.39% FACS recovery, 39.94 ± 6.30%, mean ± s.e.m., 'place' mean = 34.63%, 'place' median = 25.0%; 'silent' mean = 46.59%, silent median = 45.09%). (**D**) Volcano plot of Meso-seq differential expressed gene (DEG) analysis for 'place' and 'silent' cells (significantly different genes are shown in orange and blue. Orange: enriched in place cells; blue: enriched in silent cells). (**E**) Meso-seq MA plot depicting DeSeq2 normalized gene counts versus log2 fold change of silent/place samples. Genes that are significantly different are labeled in orange and blue (same as above). Genes shown in panels *F* & *G* are highlighted and labeled in *E*. (**F**) Bar graph showing the normalized counts for genes that are not differentially expressed (FDR adjusted q-value. *<0.05, **<0.001, ***<0.001, PyDeSeq2. Otherwise, comparisons are not significant). (**G**) Bar graph showing the normalized counts for differentially expressed genes

(FDR adjusted p-value. *<0.05, **<0.001,***<0.001, PyDeSeq2. Otherwise, comparisons are not significant). (**H**) Gene ontology analysis performed on all differentially expressed genes. Vertical line: FDR-adjusted p value of 0.05. NES = normalized enrichment score. Boxplots show the 25th, 50th (median), and 75th quartile ranges, with the whiskers extending to 1.5 interquartile ranges below or above the 25th or 75th quartiles, respectively. Outliers are defined as values extending beyond the whisker ranges.

Discussion

The comprehensive molecular-functional characterization of cortical circuits remains elusive due to the limited toolkit for correlated *in vivo* functional recording techniques and *post hoc* molecular analyses. Here, we introduced 2P-NucTag, a robust function-forward approach combining *in vivo* imaging, on-demand single-nucleus tagging, and *post hoc* transcriptomics. This pipeline seamlessly integrates 2P Ca^{2+} imaging in behaving mice, 2P phototagging of functionally identified neuronal nuclei, FACS-isolation of the tagged nuclei, and subsequent analyses of isolated nuclei with a mesoscale protocol for in-depth transcriptomics in ultra-sparse neuronal populations.

We demonstrated the utility of 2P-NucTag by selectively labeling and analyzing transcriptional profiles of two functionally orthogonal subpopulations of hippocampal PNs, 'place' cells and 'silent' cells, which remained inaccessible with existing techniques. Unexpectedly, our experiments revealed a number of genes that are putatively differentially expressed between these distinctly transient physiological cell states[35–40]. The relatively low expression levels for some of these genes indicate that further replicates may be necessary to confirm their differential expression. Nevertheless, several of the identified genes generate new hypotheses about the molecular mechanisms that underlie these two functional cell identities, which had been molecularly indistinguishable otherwise. Specifically, the marked enrichment of an inward rectifying potassium channel Kir2.2 (encoded by *Kcnj12*) in silent cells suggested that expression of this gene might reduce the excitability of hippocampal pyramidal neurons to thereby lower the activity of these cells *in vivo* and reduce their propensity to become place cells[82]. Indeed, our experiments based on ectopic expression of *Kcnj12* are consistent with this idea, and thereby implicate intrinsic excitability as a putative cellular and molecular mechanism that can influence the activity and spatial coding properties of PNs in the hippocampus. Thus, our findings on *Kcnj12* align with previous studies showing that intrinsic excitability is a major factor governing cell recruitment to a memory trace[83–86]. Future experiments will be needed to test the function of specific genes that we have identified with our tagging technique, which could reveal a non-random allocation of functional activity onto CA1 PNs during learning and experience. In particular, future application of 2P-NucTag to selectively tag PNs with highly distinct and shared coding properties, including place field propensity[28,36,87,88], recruitment to 'replay' and 'preplay' events[89–92] and participation in functionally interconnected subnetworks[69] may uncover genetic and developmental[93–98] backbones of functional heterogeneity among PNs.

Our results showed low levels of unintended PAmCherry photoactivation during functional imaging as well as limited off-target labeling. Although the activation level of these background and off-target neurons is lower and the actual targeted cells' photoactivation can be distinguished through *in vivo* imaging, FACS, and *ex vivo* confocal imaging, this presents a complicating factor e.g. when setting gating levels for FACS. Therefore, in this study, we sorted only the brightest population of cells with high levels of mCherry fluorescence (Figures 3B, S7). Future optimization of the phototagging vector and the 2P tagging parameters will help refine photoactivation specificity. Nevertheless, our proof-of-principle implementation of 2P-NucTag to

436 transcriptomically characterize functionally heterogeneous hippocampal PNs that are spatially
437 intermixed in the densely packed pyramidal cell layer demonstrates that 2P-NucTag should be
438 readily applicable to neocortical tissue with lower cell density.

439 Beyond this first application to the mouse hippocampus, 2P-NucTag will have broad appeal
440 for correlated structural, molecular, and functional analysis of neural circuits. Our approach offers
441 the ability to bridge molecular, cellular-synaptic, and functional architecture in cortical circuits
442 and facilitates the identification of candidate genes that determine the distinct circuit functions of
443 neurons. Our results with 'Recurring' place cells further demonstrate that this pipeline should be
444 potent for uncovering molecular signatures of phenomenologically described neuronal subsets
445 with distinct feature selectivity, task-related activity, and longitudinal stability that are spatially
446 intermixed in cortical circuits[21,23,25,99–103].

447 Our approach can also be extended in multiple directions. Firstly, as 2P-NucTag is
448 compatible with *post hoc* histological analysis of imaged tissue, it can be combined with spatially
449 resolved transcriptomics[17,18,104,105] following automated registration between *in vivo* and *post hoc*
450 images[106,107]. Secondly, *ex vivo* electrophysiological recordings from tagged cells will allow for
451 detailed *ex vivo* physiological and anatomical characterization of the *in vivo* tagged cells[9–12].
452 Thirdly, while we opted to use Meso-seq for our transcriptomic analyses, our pipeline is
453 compatible with sc/snRNA-seq, given the single-cell resolution achieved through targeted
454 photoactivation. Fourthly, further optimization of phototagging with multi-color fluorophores may
455 enable simultaneous labeling of multiple functionally defined cell types in the same animal, while
456 cytosolic tags[48] can promote anatomical labeling of subcellular axonal or dendritic compartments
457 for downstream structural and connectivity analyses. Lastly, the on-demand nature of
458 photoactivation and its days-long stability following single photoactivation makes our pipeline a
459 valuable tool for precise analysis of transcriptional trajectories following cellular plasticity events
460 during, for example, behavioral learning[53,74,108,109].

461 In summary, our novel phototagging approach expands our understanding of the
462 fundamental relationship between the molecular and functional architecture of mammalian cortical
463 circuits and allows for the identification of candidate genes that determine the distinct circuit
464 functions of seemingly homogeneous populations of neurons. Beyond the proof-of-principle
465 implementation to hippocampal circuits, our approach provides a general framework and roadmap
466 for linking genes to cells across neural circuits and model organisms.

Materials and Methods

Animals

All animal care and experiment procedures were in accordance with the guidelines of the National Institute of Health. Animal protocols were approved by the Columbia University Institutional Animal Care and Use Committee and the Weizmann Institute of Science Institutional Animal Care and Use Committee. Mice were group-housed under normal lighting conditions in a 12-hour light/dark cycle. *Ad libitum* water was provided until the beginning of training for the spatial navigation task.

Plasmids and Viral Constructs

pAAV-CW3SL-GCaMP7f-4Ala-H2B-PAmCherry was generated by standard cloning techniques. GCaMP7f was PCR-amplified from Addgene plasmid #104492 with a 3' Primer that contained sequences encoding four Alanine residues and the P2A sequence (both in frame with the coding sequence of GCaMP7f). H2B-PAmCherry was amplified from Addgene plasmid #133419. The PCR products were then subcloned by Gibson-assembly into Addgene plasmid #61463 after removing EGFP from this plasmid by restriction with ClaI and EcoRI. The sequence of the cloned plasmid was validated by Sanger sequencing and GCaMP7f + 4xAla, P2A and H2B-PAmCherry were all found to be in frame. The plasmid was packaged into AAVDJ at a viral titer of 7.26E+15 essentially as described[55].

pAAV-hSyn-FLEX-Kir2.2$_{WT}$-T2A-mRuby3 and pAAV-hSyn-FLEX-Kir2.2$_{Mut}$-T2A-mRuby3 were generated at GenScript Inc. by synthesizing the respective inserts (Kir2.2$_{WT}$-T2A-mRuby3, Kir2.2$_{Mut}$-T2A-mRuby3) and cloning them with standard cloning techniques into the viral backbone AAV phSyn1(S)-FLEX-tdTomato-WPRE (Addgene plasmid # 51505). The gene encoding the Kir2.2 channel was synthesized based on Genbank accession number #NM_001267593 (i.e., isoform2 of mouse *Kcnj12*), and mRuby3 based on GenBank accession number #KX987299.1. The plasmid was then packaged into AAVDJ at a viral titer of 1E+13. The strategy of generating active WT channels and Mut control channels were similar to those used in previous studies to generate active and inactive forms of Kir2.1[56,110,111].

pAAV-EF1a-H2B-PAmCherry was generated by standard cloning techniques. H2B-PAmCherry was amplified from Addgene plasmid #133419 with the relevant sticky ends. The PCR product was then subcloned using Enzymatic ligation into Addgene plasmid #203845 after removing fDIO-mRuby3-2A-dCre from this plasmid by restriction with SalI and EcoRV. The sequence of the cloned plasmid was validated by Sanger sequencing and H2B-PAmCherry were found to be in frame. The plasmid was packaged into AAVDJ at a viral titer of 3.96E+13.

Surgery

All procedures were performed with mice under anesthesia using isoflurane (4% induction, 1.5% maintenance in 95% oxygen). Mice's body temperature was maintained using a heating pad both during and after the procedure. Surgeries were performed on a stereotaxic instrument (Kopf Instruments). Before incision, mice were given subcutaneous meloxicam, as well as bupivacaine at the incision site. Doses were calculated based on the animal's weight. An incision above the skull was made to expose bregma and lambda for vertical alignment. Skull surfaces were cleaned and scored to improve dental cement adhesion. For viral injection, a glass capillary loaded with rAAV is attached to a Nanoject device (Drummond Scientific).

512 For hippocampal CA1 2P imaging mice except those described in Figure S12 and S13, viruses
513 were injected unilaterally in the left dorsal CA1 at 4 depths using the coordinates: -2.2 AP, -1.75
514 ML, and -1.2, -1.1, -1.0, -0.9 DV (relative to dura). At each depth, 75nl of AAVDJ-CW3SL-
515 GCaMP7f-4Ala-H2B-PAmCherry was injected. After injection, surgical sites were closed with
516 sutures. Three days after injection, the skull was exposed and a 3mm craniotomy was made
517 centered at the same coordinate of the injection site. Dura was removed, and the cortex was slowly
518 aspirated with continuous irrigation of cold 1X PBS until the fiber tract above the hippocampus
519 was visible. A 3-mm imaging cannula fitted with a 3mm glass coverslip was implanted over the
520 craniotomy site. Cannulas were secured by Vetbond. A custom titanium headpost for head-fixation
521 was secured first with C&B Metabond (Parkell) and then dental acrylic. At the end of each
522 procedure, the mice received a 1.0 ml saline injection subcutaneously and recovered in their home
523 cage with heating applied. Mice were monitored for 3 days after the procedure.
524 For mice used in Figure S12, 100nl of AAVDJ-hSyn-FLEX-Kir2.2$_{WT/Mut}$-T2A-mRuby3 + AAV9-
525 hSyn-GCaMP8s + AAV1-hSyn-cre were injected at 4 depths using the coordinates: -2.2 AP, -1.75
526 ML, and -1.2, -1.1, -1.0, -0.9 DV (relative to dura). All other surgery procedures are the same as
527 described above.
528 For mice used in Figure S13, 100nl of AAVDJ-Ef1a-H2B-PAmCherry + AAV9-hSyn-GCaMP8s
529 were injected at 4 depths using the coordinates: -2.2 AP, -1.75 ML, and -1.2, -1.1, -1.0, -0.9 DV
530 (relative to dura). All other surgery procedures are the same as described above.
531 For all visual cortex experimental mice, virus was injected unilaterally in the left visual cortex
532 using the coordinates: -2.7 AP, -2.5 ML, and -0.3 DV. 2-3 injections of 300 nl of virus were made
533 using a beveled glass micropipette to target layer 2/3 of the cortex at a rate of 65 nl/min using a
534 microsyringe pump (UMP3T-2, World Prevision Instrument). A 4 mm craniotomy was made
535 above the visual cortex, and a coverglass and custom-made, 3D printed head post painted black to
536 allow for head fixation during imaging was glued to the skull using cyanoacrylate glue (Krazy
537 Glue). Following surgery, animals were administered with analgesic (0.1 mg/kg of buprenorphine
538 and 5 mg/kg of Carprofen). After initial recovery on a heating pad (RWD Life Science), mice were
539 returned to their homecage and monitored for post-op care.
540
541
542 **Behavior paradigm**
543 Mice were first water-deprived and habituated to handling and head fixation at least 7 days after
544 implant surgery. For behavior experiments in Figure 2 and Figure S13, mice were exposed to a 4-
545 m-long linear virtual reality (VR) corridor[65–67] that stayed consistent in training and recording. For
546 behavior experiments in Figure S12, mice were first exposed to a 4-m VR corridor without features
547 ('blank' environment), and they were exposed to the feature-rich VR environment same as the
548 ones used in Figure 2 and Figure S13 on the first day of 2P functional imaging. At the end of the
549 environment, an inter-trial interval of 2 seconds of blank screen was included before the start of
550 the next lap. For the next 10-14 days, mice were trained to run through the virtual environment
551 and lick for a 5% sucrose reward. The rewards were first randomly distributed across the
552 environment, and the number of rewards was slowly reduced from 30 at the beginning of the
553 training to 2 when the mouse was deemed ready for recording. The final reward location was fixed
554 toward the end of the VR environment. Mice were trained to run at least 30-60 laps in the
555 environment. During behavioral imaging, mice were imagined during a single VR session (range:
556 18-40 min, 26 ± 3 min, n = 9 mice).
557

558 ***In vivo* two-photon imaging and data processing**
559 For 2P imaging of dorsal hippocampal CA1, 2P functional imaging was conducted using an 8-kHz
560 resonant scanner (Bruker) and a 16x near-infrared (NIR) water immersion objective (Nikon, 0.8
561 NA, 3.0-mm working distance). For population imaging in Figure 2 and Figure S12, a field of
562 view of 700 μm x 700 μm was acquired, and for population imaging in Figure S13, a field of view
563 of 420 μm x 420 μm was acquired. All imaging were done at 30 Hz, 512 x 512 pixels using a 940-
564 nm laser (Chameleon Ultra II, Coherent, 45-91 mW after the objective). Red (PAmCherry) and
565 green (GCaMP7f) channels were separated by an emission cube set (green, HQ525/70 m-2p; red,
566 HQ607/45 m-2p; 575dcxr, Chroma Technology), and fluorescence signals were collected with
567 GaAsP photomultiplier tube modules (7422P-40, Hamamatsu). Following the acquisition of two-
568 photon imaging data, Ca^{2+} imaging data was structured and aligned with behavior data using the
569 SIMA analysis package[112]. CA1 ROIs were detected using the Suite2p (v0.14.2) package[113]. To
570 allow detection of all potential ROIs regardless of their activities during the recording, Suite2p
571 was run with Cellpose ('anatomical_only')[114] for the ROI detection step. The pre-trained cyto2
572 model included in the published Cellpose package was used for ROI detection. When capturing
573 two-photon z-stack images of photoactivated PAmCherry nuclei, a fixed wavelength 1070-nm
574 laser (Fidelity-2W, Coherent) was used for excitation.
575 For 2P imaging of primary visual cortex, a two-photon microscope equipped with a 12 kHz
576 resonant-galvo scanhead (Bergamo microscope, ThorLabs) was used with a Ti:Sapphire laser
577 (MaiTai DeepSee, Spectra Physics). Imaging data was concatenated, registered, ROIs were drawn
578 and fluorescence was extracted using Suite2p. Following this, all recordings were analyzed using
579 custom software written in house in MATLAB (MathWorks). F signals were neuropil corrected
580 and aligned to timing of visual stimulation using frame time signals collected in Clampex
581 (Molecular Devices) during recording sessions and averaged across repetitions. Field of views
582 (FOVs) were mapped in order to determine the location of V1 and best imaging area for recordings
583 per animal. Receptive fields were mapped by presenting patches of drifting sinusoidal gratings
584 spaced on a 3 by 4 grid of the monitor. Stimuli were presented for 1 s at 0, 100% contrast and 0.04
585 cpd with an interstimulus interval of 4 s. FOVs were selected based on receptive field mapping
586 and percentage of visually responsive neurons in the area.
587
588 **Visual stimulation before and after phototagging**
589 Visual stimuli were generated using the MATLAB Psychophysics toolbox
590 (http://psychtoolbox.org/) and presented on a gamma-corrected LCD screen. The screen was
591 positioned 20 cm from the contralateral eye of the recorded hemisphere. Stimuli were presented
592 for 1 s with an interstimulus interval of 4 s during which a gray screen of mean luminance was
593 presented. Visual stimuli consisted of full-field sinusoidal drifting bar gratings with a temporal
594 frequency of 2 Hz. Varying directions (equal spacing of 30) were presented in a pseudorandom
595 order with 24-25 repetitions per stimulus type.
596
597 ***In vivo* two-photon phototagging**
598 Photoactivation was conducted using a three-dimensional random-access acousto-optical (3D-
599 AOD) microscope (3D Atlas, Femtonics)[19,54]. Mice were head-fixed and anesthetized with
600 isoflurane to minimize motion and increase the spatial precision of phototagging. The same 16x
601 NIR water immersion objective was used to find the same field of view as in the functional
602 recordings. Photoactivation was performed at 810-nm (Chameleon Ultra II, Coherent). Two-
603 photon images of the mCherry red fluorescence were taken before and after photoactivation using

604 a 1040-nm excitation laser (Alcor 1040-5W, Spark Lasers). Red (mCherry) and green (GCaMP7f)
605 channels were separated by an emission cube set (green, HQ520/60 m-2p; red, HQ650/160 m-2p;
606 565dcxr, Chroma Technology), and fluorescence signals were collected with GaAsP
607 photomultiplier tube modules (7422P-40, Hamamatsu). Two-photon images of the mCherry red
608 fluorescence were taken before and after photoactivation using a 1040-nm excitation laser (Alcor
609 1040-5W, Spark Lasers). For photoactivation, a 7 x 7 μm, 0.1 μm /pixel scanning pattern was
610 placed on the cell to be photoactivated. Each pixel was activated for a total dwell time of 1.3 ms
611 with a laser power of 40 mW. This gave the total scanning time of each cell at 6,370 ms. Following
612 photoactivation, a z-stack was taken for each mouse to assess the photoactivation efficacy.
613 For phototagging of 'place cells' and 'silent cells', photoactivation experiments were conducted a
614 day after functional recording sessions. For phototagging of 'Day 0 cells' and 'Recurring cells',
615 photoactivation experiments were conducted the same day as functional recording sessions. The
616 imaging field of view of 700 μm x 700 μm was matched between the 3D-AOD microscope and
617 the time-averaged GCaMP image from functional recording. After confirming the same field of
618 view as functional imaging, the viewport was zoomed in to a dimension of 250 x 250 μm for more
619 effective identification of targeted cells according to the generated spatial masks. Following
620 photoactivation of all cells, a z-stack image was taken for each mouse to confirm the tagging
621 accuracy. Mice were given *ad libitum* water after functional imaging for at least 12 hours before
622 photoactivation. During the session, mice were monitored every 10 min for breathing rate and
623 reflexes. Heating and eye ointment were applied. Following the photoactivation, mice were
624 returned to the home cage to recover with a heating pad.
625 For phototagging of neurons in the primary visual cortex, a 405 nm LED light was used to
626 illuminate the field of view for 30 seconds to achieve photoactivation of most of the infected
627 neurons, and photoactivation of neurons were confirmed by recording in the red channel using a
628 1040 nm laser before and after photoactivation.
629
630 **Tissue dissociation and preparation of nuclei for FACS**
631 For all animals used in this manuscript, tissue collection was performed at the same time of the
632 day (5 pm) and at least one hour after the photoactivation. Mice were euthanized using CO_2. The
633 headpost and metal cannulas were removed. Dorsal CA1 of the hippocampus was collected by first
634 using a 3-mm biopsy punch to cut a circular section of tissue the same size as the craniotomy. A
635 microspatula was used to remove the shallow section of tissue that contained dorsal CA1. The
636 tissue was placed in a 1.5 ml RNase-free Eppendorf tube and snap-frozen in liquid nitrogen.
637 Tissues were stored at -80 °C until the start of the nuclei isolation.
638 Nuclei were prepared for FACS sorting essentially as previously described (*46*). In short, to isolate
639 the nuclei, each collected tissue was transferred to a dounce tissue homogenizer (DWK Life
640 Sciences) with 1ml of homogenization buffer (10 mM Tris Buffer, 250mM Sucrose, 25 mM KCl,
641 5mM $MgCl_2$, 0.1mM DTT, 0.1% Triton X-100, 1X Protease Inhibitor Cocktail, and 40U/μl
642 RNAsin Plus RNase Inhibitor in nuclease-free water). Loose and tight pestles were used to break
643 apart the tissue 10 times each. Following the homogenization, 1 ml of homogenization buffer was
644 added to each dounce, and the homogenate was pipetted up and down to further break apart tissue
645 before being passed through a 30 μm cell strainer (Miltenyi Biotec) and collected in a 15 ml conical
646 tube.
647 The homogenate was centrifuged at 4 °C, 700g for 8 min. The supernatants were then removed
648 from the visible nuclei pellet. The nuclei pellet was resuspended with 800 μl of blocking buffer
649 (1X PBS, 1% BSA, and 40 U/μl RNasin Plus RNase Inhibitor in nuclease-free water). The

650 resuspension was incubated on ice for 15 min and transferred to a 1.5 ml tube. 2 µl of CoraLite
651 Plus 488-conjugated NeuN Monoclonal antibody (Proteintech) was added to the resuspension, and
652 incubated on an orbital rotator at 4 °C for 30 min. After incubation, nuclei were centrifuged at 4
653 °C, 700 g for 8 min. The supernatant was removed, and the nuclei pellet was resuspended with
654 1000 µl of blocking buffer. DAPI was added to the suspension at a final concentration of 0.001
655 mg/ml, and the samples were passed through a 40- µm Flowmi Cell Strainer (Bel-Art). All samples
656 were kept on ice until the start of FACS.
657
658 **Fluorescence-activated cell sorting (FACS)**
659 The sorting was performed at the Zuckerman Institute Flow Cytometry Core using a MoFlo Astrios
660 Cell Sorter (Beckman Coulter). Event rates were kept between 5000-10000 events per second. The
661 cell sorter uses a linear array of lasers ordered as 640 nm, 488 nm, 561 nm, 532 nm, 405 nm and
662 355 nm from top to bottom. For experiments described in this manuscript, 488 nm, 561 nm and
663 405 nm lasers were used to detect the fluorescence of NeuN, mCherry and DAPI respectively. A
664 gating control sample was used to set the gates for DAPI, NeuN and mCherry. Dissociated nuclei
665 were passed through the cell sorter to collect those with high mCherry signals. Bright and Dim
666 mCherry gates were determined after the first 5000 events of DAPI-positive nuclei. Gating was
667 set to collect only the sparse and bright population that showed a high mCherry signal, and these
668 events were collected as the photoactivated nuclei ('Bright' mCherry). Nuclei were collected into
669 SMART-Seq CDS sorting buffer that contains 1X lysis buffer, SMART-Seq Oligo-dT and RNase
670 inhibitor. All sorted samples were kept on dry ice as recommended by the SMART-Seq protocol
671 until the start of first-strand synthesis. To increase the likelihood of collecting nuclei in this ultra-
672 sparse population, aborted events for 'Bright' mCherry and all events for other positive mCherry
673 were collected into the blocking buffer (200 ml). This suspension was passed through the sorter
674 again with the same fluorescence gating following the completion of the first sorting to capture
675 the bright nuclei.
676
677 **Meso-seq**
678 We followed the previously published Meso-seq protocol[55] with minor modifications. Sorted
679 nuclei were collected in a lysis buffer following the SMART-Seq mRNA LP protocol. Reverse
680 transcription for cDNA was followed by cDNA amplification using 17-18 PCR cycles. Purified
681 cDNA was prepared for sequencing the library using the SMART-seq Library Preparation Kit.
682 Libraries were amplified using 14 PCR cycles. The concentration of the final library was
683 determined using a Qubit3.0 Fluorometer (Invitrogen), and the average DNA fragment size was
684 determined using a Bioanalyzer (Agilent). Sequencing was performed on a NextSeq 2000
685 sequencer with P2-100 reagents (Illumina). Libraries were diluted and pooled according to the
686 recommendation of the sequencing kit.
687
688 ***Ex vivo* electrophysiology in acute hippocampus slices**
689 Mice were transcardially perfused with ice-cold sucrose dissection media (26 mM NaHCO3, 1.25
690 mM NaH2PO4, 2.5 mM KCl, 10 mM MgSO4, 11 mM glucose, 0.5 mM CaCl2, 234 mM sucrose;
691 340 mOsm). Brains were then dissected and sliced, while being kept in ice-cold sucrose dissection
692 media, into coronal sections (300 µm thick) containing the hippocampal CA1 using a Leica
693 VT1200S vibratome. Slices were incubated in high osmotic concentrated artificial cerebrospinal
694 fluid (aCSF) (28.08 mM NaHCO3, 1.35 mM NaH2PO4, 132.84 mM NaCl, 3.24 mM KCl, 1.08
695 mM MgCl2, 11.88 mM glucose, 2.16 mM CaCl2; 320 mOsm) at 32°C for 30 minutes immediately

696 after slicing. Then, slices were incubated in normal osmotic concentrated artificial cerebrospinal
697 fluid (26 mM NaHCO3, 1.25 mM NaH2PO4, 123 mM NaCl, 3 mM KCl, 1 mM MgCl2, 11 mM
698 glucose, 2 mM CaCl2; 300 mOsm) at 32°C for 30 minutes and subsequently at room temperature.
699 All solutions were saturated with 95%-O2/5%-CO2, and slices were used within 6 hours of
700 preparation. Whole-cell patch-clamp recordings were performed in aCSF at 32°C from neurons in
701 the hippocampus. Recording pipettes were pulled from borosilicate glass capillary tubing with
702 filaments (OD 1.50 mm, ID 0.86 mm, length 10 cm) using a P-700 micropipette puller (Sutter
703 Instruments) and yielded tips of 3–5 MΩ resistance. Recordings were sampled at 20 kHz and
704 filtered at 3 kHz. Data were acquired via Clampex10 using a Multiclamp 700B amplifier and
705 digitized with an Axon Digidata 1550B data acquisition board (Axon Instruments). Tagged
706 neurons were identified based on mCherry nuclear fluorescence using a pE-300 white MB LED
707 light (CoolLED) with GYR (525-660nm) spectrum, combined with an Olympus Cy5 Filter Cube
708 Set (ex. 604-644nm; em. 672-712nm).
709 To ensure that the recorded cells were indeed phototagged neurons, Alexa 594 Hydrazide (10uM)
710 was added to the internal solution to allow co-localization of the fluorescence of the tagged neuron
711 to the one that was patched using confocal imaging in PFA(4%)-fixed slices.
712 For measuring the intrinsic properties, the following internal solution was used: 135 mM k-
713 gluconate, 4mM KCl, 10mM HEPES, 10mM Pcreatine, 4mM Mg-ATP, 4mM GTP-Na and 2mM
714 Na2-ATP. Intrinsic properties were calculated by giving 1.2s long current steps (20pA).
715
716 **Tissue collection and processing for *in situ* hybridization**
717 Mice were anesthetized with isoflurane and transcardially perfused with 20 mL of ice-cold 0.01M
718 phosphate base saline (PBS, Sigma) followed by 20 mL ice-cold 4% paraformaldehyde (PFA,
719 Electron Microscopy Sciences) in PBS. Brains were post-fixed in 4% PFA for 24 hours and then
720 saturated with a 10%, 20%, and 30% sucrose solution sequentially over 48 hours until they sunk
721 to the bottom of each successive solution. 30% Sucrose-saturated brains were then embedded in
722 OCT (Optimal Cutting Temperature Compound, Sakura, cat#4583), frozen, stored overnight at -
723 80 °C, and sliced transversely at 20 µm thickness with a cryostat. Sections were stored at -80 °C
724 on slides and used for RNAScope *in situ* hybridization.
725
726 **RNAScope Fluorescent In Situ Hybridization (FISH)**
727 20 µm fixed frozen sections of the frozen tissue block were taken and the RNAScope™ Multiplex
728 Fluorescent Reagent Kit v2 – User Manual was followed (cat#: 323100). The *Kcnj12* targeting
729 probe was designed for *Mus musculus* and generated by Advanced Cell Diagnostics Inc (C3: Cat
730 No. 525171, Entrez Gene ID: 16515, GenBank Accession #: NM_010603.6), and same for the
731 *Pcdha8* probe (C1; Cat No. 841011, Entrez Gene ID: 353235, GenBank Accession #:
732 NM_201243.1). Slides were sequentially dehydrated using ethanol solutions of increasing
733 concentrations (50%, 70% and 100%) for 5 min each at RT. 5-8 drops of H_2O_2 were added to each
734 sample, followed by a 10 min incubation at RT. After rinsing with distilled water, antigen retrieval
735 was performed for 5 min at 99°C (shorten from the manufacturer's recommendation to preserve
736 PAmCherry fluorescence while maintaining RNAscope signal). To digest sections, RNAscope
737 Protease III was applied to the sections for 30 min at 40°C. The probes were hybridized for 2 h at
738 40°C and amplified with AMP1 (30 min), AMP2 (30 min), AMP3 (15 min); each was incubated
739 at 40°C. The probe was fluorescently tagged with 1:2000 TSA Vivid Fluorophore 650 (PN
740 323273). Slides were counterstained with DAPI for a nuclear stain to identify viable cells and

741 mounted in ProLong Gold Antifade Mountant. 20 µm sections were imaged in 3 µm z-steps using
742 an inverted confocal microscope with 20x air objective (A1 HD25, Nikon Instruments Inc.).
743
744 **Data analysis**
745 **Quantification and Statistical Analysis**
746 All statistical details for comparisons are described in the text. No statistical methods were used
747 to determine sample sizes. Boxplots show the 25th, 50th (median), and 75th quartile ranges with the
748 whiskers extending to 1.5 interquartile ranges below or above the 25th or 75th quartiles,
749 respectively. Outliers are defined as values extending beyond the whisker ranges. For comparisons
750 between two populations with non-normal distributions, the Mann-Whitney U test was used. For
751 comparisons between gene expression datasets, the Wald test followed by multiple corrections via
752 the Benjamini and Hochberg method was used as described in PyDESeq2[115].
753
754 **Event detection**
755 Fluorescence GCaMP traces were deconvolved using OASIS for fast nonnegative
756 deconvolution[116]. As in ref.[117], these putative spike events were filtered at 3 median absolute
757 deviations (MAD) above the raw trace, using a predetermined signal decay constant of 400 ms.
758 The binarized signal was used to qualify whether a neuron was active at the respective frame. In
759 our analysis, we do not claim to uncover true spiking events in these neurons but use deconvolution
760 for denoising and diminishing Ca^{2+} autocorrelation.
761
762 **Spatial tuning curves**
763 The virtual environment was divided into 100 evenly spaced bins (4 cm), which were then utilized
764 to bin a histogram of each cell's neuronal activity. Neuronal activity was filtered to include activity
765 from when the animal was running above 3 cm/s and to exclude activity during the 2-sec
766 teleportation at the end of the 4-m track. The spatial tuning curves were normalized for the animal's
767 occupancy and then smoothed with a Gaussian kernel (σ = 12 cm) to obtain a smoothed activity
768 estimate.
769
770 **Place cell detection**
771 Place fields were detected by identifying locations in the virtual environment where a neuron was
772 more active than expected by chance. We circularly shifted each neuron's deconvolved spike trace
773 and recomputed the smoothed, trial-averaged spatial tuning curve of the shifted trace to generate
774 a shuffled null tuning curve per cell. We repeated this procedure 1000 times in order to calculate
775 the 95th percentile of null tuning values at every spatial bin to generate a threshold for a $p<0.05$
776 significance curve. Spatial tuning curves that surpassed the null threshold were marked as
777 candidate place fields, and the place field width was calculated as the total bins where the tuning
778 curve exceeded the shuffled null tuning curve. To restrict our analysis to neurons with specific
779 firing fields, we additionally required that place fields have a width greater than 8 cm and less than
780 one-third of the virtual environment (1.3 m). To ensure that the place field activity was stable, we
781 also required that all place cells had activity for at least 20 laps.
782 If the binarized signal trace for a cell did not have any detected events via OASIS deconvolution,
783 the cell was classified as silent.
784 For experiments described in Figure S12, five consecutive days of recording were first
785 concatenated as one image sequence and Suite2P was used for motion correction and ROI-
786 detection. They were then separated into recording for each day for analysis. Place fields detection

were performed for each cell for each recording days, and same ROI number were used across days. Cells with place field for at least 4 out of 5 days were classified as 'Recurring' cells. 'Day 0' cells were place cells with place fields on the first recording day, done in a separate set of animals.

PAmCherry fluorescence quantification

(Figure 1C,D)

Red PAmCherry fluorescence was calculated as the tagged nuclei fluorescence versus the background fluorescence of nearby untagged nuclei for the image taken post-tagging. This was intentional to control for periodic two-photon imaging at 940 nm that may cause an increase in fluorescence for every cell in the FOV.

Fluorescence intensity distribution analysis

(Figure 1F, right)

Red PAmCherry tagged nuclei were segmented using Cellpose with manual curation performed within the Cellpose GUI for the max axial projections of the *ex vivo* z-stack (excitation: 568 nm nm) and *in vivo* z-stack (1070 nm) to generate masks. The masks were used to segment the 3-D volumes of each cell and the respective fluorescence profiles were normalized and aligned based on the peak value. The average and standard error were computed based on the aligned fluorescence profiles of the cells from the respective *in vivo* and *ex vivo* volumes.

Two-photon background excitation fluorescence quantification

[Figure 2G(2P imaging), Figure S4F (2P imaging)]

Changes in PAmCherry red fluorescence due to two-photon fluorescence excitation at 940 nm from functional recordings were examined. By taking the average fluorescence of the pre-imaging red channel image and post-imaging red channel image detected at 1070 nm, ΔF/F was computed using the change in fluorescence between the average post-imaging red image and pre-imaging red image divided by the pre-imaging red image average [(post – pre) / pre].

Tagged and Off-target Fluorescence Change Quantification

[Figure 1G (target, off-target), Figure S4F (target, off-target)]

Tagged nuclei were segmented using Cellpose with manual curation performed within the Cellpose GUI for the max axial projection of the *in vivo*-stacks from each mouse to generate masks. These masks were used to segment a 3D volume for each nucleus that was targeted across all mice. The number of off-target nuclei was manually quantified laterally and axially per targeted nuclei. Masks for off-target nuclei were hand-drawn on the max axial projection to exclude the targeted nuclei and were at most 2 nuclei bodies away. Experimental background fluorescence masks were drawn on the surrounding areas with successfully tagged nuclei and excluded all targeted and off-target nuclei.

The fluorescence values for all tagged and off-target nuclei were percentile-filtered to exclude the lower 10% of fluorescence values to account for vignetting effects and mask inhomogeneities over the max axial projection. Background fluorescence levels were selected in the areas of field of view without tagged nuclei. The percentile filtered fluorescence values for tagged and off-target nuclei were averaged, and the ΔF/F was computed by taking the difference between the average tagged or off-target fluorescence value and the average background fluorescence and then normalizing by the average background fluorescence [tagged: (tagged – background)/background;

off-target: (off-target – background)/ background]. Note this background value is distinct from the one described in the two-photon background excitation fluorescence quantification.

GCaMP quantifications

[Figure S1AB, Figure S4I]

Frequency: The total number of deconvolved events by OASIS was normalized by the total duration of the recording.

For each cell, the average transient was segmented within a 15-second time window and computed by averaging along aligned deconvolved spike times. If multiple detected events were within 50 frames, the events were treated as a single transient. A cell was only used if there were at least 3 detected transients within the total trace to exclude cells without obvious GCaMP-Ca^{2+} dynamics. For each average transient, we computed the median value based on 5 seconds pre peak transient and the range 5-10 seconds after the peak transient (given that the average transient took significantly less than 5 seconds to resolve) to act as the baseline.

Amplitude: The difference between the max value of the average transient and the baseline value was computed

Half-Rise Time: The time between the half-max value prior to the max and the max value of each transient was computed. We excluded cells where the average half-max value was not observed prior to the transient and performed 99th percentile filtering to remove extreme outliers. Due to sampling rate limitations, we cannot comment on the true half-rise time, so these are approximations.

Half-Decay Time: We computed the time between the max and the half-max value following the transient peak. To remove extreme outliers, we performed 99th percentile filtering.

Visually evoked neural activity

[Fig. S6]

Visually evoked responses were calculated as the mean ΔF/F during visual stimulus presentation:

$\Delta F/F=(F-F0)/F0$

Where F0 was calculated as the mean fluorescence during the 1 second preceding the visual stimulus. To determine if a cell was visually responsive, a one-way non-parametric ANOVA (Kruskall-Wallis) was computed comparing the evoked responses to baseline fluorescence. An additional non-parametric test was performed between the activity during the interstimulus interval and during presentation of the preferred visual stimulus (Wilcoxon Rank Sum test , $p < 0.05$).

Neurons were included in further analyses if they were visually responsive both before and after photoactivation, and if they were determined to be successfully photoactivated.

Orientation selectivity was calculated using a calculation of the global orientation selectivity index (gOSI):

$gOSI=|(\sum R(\theta)\times e^{2i\theta})/\sum R(\theta)|$

Where R(qk) is the response to angle qk. To calculate the population average, responses of each cell were normalized to their maximum response and artificially centered to 0. Normalized responses of cells were averaged and fitted using a double Gaussian:

$R=C+ R_{pref}*e^{(-(\theta- \theta_{pref})^2/(2*\sigma^2))} + R_{null}*e^{(-(\theta_{null}- \theta_{pref})^2/(2*\sigma^2))}$

Where C is a constant offset, Rpref is the response to the stimulus that produced the maximum response and Rnull is the mean response to the opposite direction: Orientation preference was calculated as the orientation that elicited the highest dF/F value according to the fit of the gaussian tuning curves.

Image denoising

To correct for vertical scanning artifacts, we utilized combined wavelet and Fourier filters described in ref.[118] [github: https://github.com/DHI-GRAS/rmstripes]. Symlet 20 wavelets were used with varying levels of decomposition (2-5) for discrete wavelet transform to perform vertical striping correction in static images.

***In vivo* and *ex vivo* image registration**

The *in vivo* and *ex vivo* images were transformed into 3D volumetric images for registration. The *in vivo* sequential images were concatenated across the z direction, i.e., depth, stacking the 2D images into a volumetric representation using MATLAB. The *ex vivo* images composed of 2D slices in each section were concatenated into 3D volumetric data using a stitching algorithm developed as a precursor for automatic *ex vivo* and *in vivo* registration[106] [github: https://github.com/ShuonanChen/multimodal_image_registration]. The discontinuity between *ex vivo* sections result in an unknown spatial correlation between them, requiring registration between sections. Common cells between sections (i.e., sections one and two) were used as reference markers for registration. The common cells were manually selected using a Napari GUI in Python and were utilized as reference markers to inform the scaling and affine transformations to be applied. The scaling and affine transformations were run automatically, transforming the second section to align with the first section. In the scaling transformation, the relative distances between cells in a section were compared to the cells in the first section, inducing an enlargement or shrinkage of the second section to match the first. In the affine transformation, the second section was geometrically transformed to align correctly with the first section. The transformations were obtained and applied to each slice in each section, and then each slice was concatenated together across the z direction to form a volumetric image.

The *in vivo* and *ex vivo* 3D images were then adjusted to have a uniform pixel size in all dimensions (1 μm in x,y and z), ensuring matching FOVs, and equivalent resolution across both images. Time-averaged representations of *in vivo* and *ex vivo* volumetric stacks were attained by employing maximum intensity projection (MIP) representations in FIJI, compressing the stacks into 2D images[119]. The *in vivo* and *ex vivo* registration was carried out using a non-rigid registration algorithm for the (i) 3D volumetric stacks and (ii) MIP (2D) images. All cells common to both *in vivo* and *ex vivo* images were manually selected as the centroid of each cell using a Napari GUI in Python. The common cells were utilized as features to inform the scaling, affine transformation, and deformation transformation, which were applied to the *ex vivo* image. The scaling and affine transformations were run automatically. In the scaling transformation, the distances between the cells in the *ex vivo* image and matching cells in *in vivo* induce enlargement or shrinking of the *ex vivo* image to match the *in vivo* image. In the affine transformation, the *ex vivo* image was geometrically transformed to align with the *in vivo* image using the matching cells. The images in the GUI are updated to reflect the changes induced by the scaling and affine transformation. The deformation transformation uses a vector field, smoothed with Gaussian filtering, to move cells and deform the image, ensuring features in the transformed *ex vivo* image align with the *in vivo* image. The deformation transformation was iteratively employed, beginning with a Gaussian kernel size of 100, reducing to a kernel size of less than 10, with the user inspecting the alignment and making manual adjustments to the cell centroid position in the GUI. The completed transformed *ex vivo* image was then overlaid with the *in vivo* image.

925
926 **RNA-sequencing data analysis**
927 Sequencing data from the Illumina Sequencer was first post-processed through the Illumina
928 DRAGEN secondary analysis pipeline to de-multiplex based on a unique index for each sample.
929 RNA-seq reads were aligned to the mouse genome (mm39) using STAR[120]. Unique reads were
930 counted using HTSeq[121]. Gene counts were then normalized with trimmed mean of M values
931 (TMM) normalization. HTSeq generated reads were then analyzed for differential expression
932 using PyDESeq2[115]. Following HTSeq counts, any genes with expression in less than 3 samples
933 were discarded. FDR adjusted p values were used to determine significantly different genes. Both
934 'place' and 'silent' cell samples were analyzed against randomly tagged, function-blind, and sex-
935 matched samples generated from mouse CA1 tissue in the same way as described in this methods
936 section above. The same comparisons were made to identify differentially expressed genes for
937 'place' versus 'random', and 'silent' versus 'random'. Within this 'random' dataset, male-female
938 samples were compared to identify differentially expressed genes influenced by sex. All DEGs
939 from these comparisons were cross-referenced to find common hits.
940
941 **Gene set enrichment analysis**
942 Gene set enrichment analysis was performed on HTSeq-generated counts using the gseapy
943 package[122] in Python 3.11. Enrichment of the fifty hallmark pathways from the molecular
944 signatures database for *Mus musculus* (version 2023.2) was compared in place and silent cells.
945 Comparisons were done with t-test and 1000 permutations.
946
947 **RNAscope FISH signal quantification and statistical analysis**
948 Cell detection was performed using Cellpose, which identified individual cells based on DAPI
949 nuclear staining. This segmentation was manually curated. The detection and quantification of
950 RNAscope probe signals was performed using QuPath's Subcellular Detection tool (version 0.5.1).
951 The detection threshold was set to ensure accurate identification of signal dots. To compare mean
952 RNA expression levels between tagged and non-tagged cells, a Mann-Whitney U Test was used.
953 For non-tagged control cells, a random subset was selected from the same tissue sections and
954 CA1sublayer as the tagged cells, with the number of control cells matched to the number of tagged
955 cells for each animal.
956
957 **Acknowledgments**
958 We thank Ira Schieren and Max Wallach (Columbia, Zuckerman Institute, ZI) and Dr. Efrat Hagai
959 (Flow Cytometry Unit, Weizmann Institute of Science) for help with FACS, Columbia University
960 Herbert Irvine Comprehensive Cancer Center Molecular Pathology Shared Resources for help with
961 the Bioanalyzer, the Bendesky lab in ZI and Dr. Hadas Keren-Shaul, Revital Ronen at the
962 Weizmann, Nancy and Stephen Grand Israel National Center (G-INCPM) for help with RNA-
963 sequencing, George Zakka (Losonczy Lab) for technical support, Erica Rodriguez (Salzman lab)
964 in ZI for help with tissue processing, the Lomvardas lab in ZI for sequencing advice and help, the
965 Gogos lab in ZI for molecular bench space, the Polleux lab in ZI for help with cell counter and
966 confocal microscopy. We thank Franck Polleux, Joseph Gogos, Steven A. Siegelbaum, and Darcy
967 Peterka (Columbia, ZI) for feedback on the manuscript.
968
969 **Funding**

SAH is supported by the Burroughs Wellcome Fund. DK is supported by a fellowship from the Israel Ministry of Absorption (IMOAb) and by the Horowitz Foundation. AL is supported by NIMHR01MH124047, NIMHR01MH124867, NINDSR01NS121106, NINDSU01NS115530, NINDSR01NS133381, NINDSR01NS131728, NIARF1AG080818. IS is supported by an ISF personal grant (2354/19) and a BSF US-Israel binational grant (2021281) and he is the incumbent of the Friends and Linda and Richard Price Career Development Chair and a scholar in the Zuckerman STEM leadership program.

Author contributions:

Conceptualization: JS, BN, DK, AL, IS
Methodology: JS, BN, DK, BR, SAH, ET, KCK, MECP, HCY, BMS, AX
Investigation: JS, BR
Software: BR, JS, TSM, CKO, EV
Formal analysis: JS, BR, TSM, ET, AL
Validation: JS, BN, DK, KCK, BR
Visualization: JS, BR, TSM, SAH, CKO, ET, MECP, KC-KM
Data curation: JS, BR, ET, TSM
Funding acquisition: AL, IS
Resources: AL, IS
Project administration: AL, IS
Supervision: AL, IS
Writing – original draft: JS, BN, BR, TSM, AL, IS
Writing – review & editing: all authors

Competing interests: Authors declare that they have no competing interests.

Data and material availability All data, code, and materials used to generate figures and perform statistical tests are available at Zenodo or NWB upon publication. RNA-seq data will be made freely available on NCBI GEO upon acceptance of our manuscript. Accession numbers for publicly available reagents are included in supplementary materials and methods.

References

1. Zeng, H. (2022). What is a cell type and how to define it? Cell *185*, 2739–2755. https://doi.org/10.1016/j.cell.2022.06.031.

2. Macosko, E.Z., Basu, A., Satija, R., Nemesh, J., Shekhar, K., Goldman, M., Tirosh, I., Bialas, A.R., Kamitaki, N., Martersteck, E.M., et al. (2015). Highly Parallel Genome-wide Expression Profiling of Individual Cells Using Nanoliter Droplets. Cell *161*, 1202–1214. https://doi.org/10.1016/j.cell.2015.05.002.

3. Tasic, B., Menon, V., Nguyen, T.N., Kim, T.K., Jarsky, T., Yao, Z., Levi, B., Gray, L.T., Sorensen, S.A., Dolbeare, T., et al. (2016). Adult mouse cortical cell taxonomy revealed by single cell transcriptomics. Nat Neurosci *19*, 335–346. https://doi.org/10.1038/nn.4216.

4. Zeisel, A., Muñoz-Manchado, A.B., Codeluppi, S., Lönnerberg, P., La Manno, G., Juréus, A., Marques, S., Munguba, H., He, L., Betsholtz, C., et al. (2015). Cell types in the mouse cortex and hippocampus revealed by single-cell RNA-seq. Science *347*, 1138–1142. https://doi.org/10.1126/science.aaa1934.

5. Harris, K.D., Hochgerner, H., Skene, N.G., Magno, L., Katona, L., Bengtsson Gonzales, C., Somogyi, P., Kessaris, N., Linnarsson, S., and Hjerling-Leffler, J. (2018). Classes and continua of hippocampal CA1 inhibitory neurons revealed by single-cell transcriptomics. PLoS Biol *16*, e2006387. https://doi.org/10.1371/journal.pbio.2006387.

6. Piwecka, M., Rajewsky, N., and Rybak-Wolf, A. (2023). Single-cell and spatial transcriptomics: deciphering brain complexity in health and disease. Nat Rev Neurol *19*, 346–362. https://doi.org/10.1038/s41582-023-00809-y.

7. Zhang, M., Pan, X., Jung, W., Halpern, A.R., Eichhorn, S.W., Lei, Z., Cohen, L., Smith, K.A., Tasic, B., Yao, Z., et al. (2023). Molecularly defined and spatially resolved cell atlas of the whole mouse brain. Nature *624*, 343–354. https://doi.org/10.1038/s41586-023-06808-9.

8. Moses, L., and Pachter, L. (2022). Museum of spatial transcriptomics. Nat Methods *19*, 534–546. https://doi.org/10.1038/s41592-022-01409-2.

9. Cadwell, C.R., Scala, F., Li, S., Livrizzi, G., Shen, S., Sandberg, R., Jiang, X., and Tolias, A.S. (2017). Multimodal profiling of single-cell morphology, electrophysiology, and gene expression using Patch-seq. Nat Protoc *12*, 2531–2553. https://doi.org/10.1038/nprot.2017.120.

10. Cossell, L., Iacaruso, M.F., Muir, D.R., Houlton, R., Sader, E.N., Ko, H., Hofer, S.B., and Mrsic-Flogel, T.D. (2015). Functional organization of excitatory synaptic strength in primary visual cortex. Nature *518*, 399–403. https://doi.org/10.1038/nature14182.

1031 11. Ko, H., Hofer, S.B., Pichler, B., Buchanan, K.A., Sjöström, P.J., and Mrsic-Flogel, T.D. (2011).
1032 Functional specificity of local synaptic connections in neocortical networks. Nature *473*,
1033 87–91. https://doi.org/10.1038/nature09880.

1034 12. Scala, F., Kobak, D., Bernabucci, M., Bernaerts, Y., Cadwell, C.R., Castro, J.R., Hartmanis, L.,
1035 Jiang, X., Laturnus, S., Miranda, E., et al. (2021). Phenotypic variation of transcriptomic cell
1036 types in mouse motor cortex. Nature *598*, 144–150. https://doi.org/10.1038/s41586-020-
1037 2907-3.

1038 13. Bock, D.D., Lee, W.-C.A., Kerlin, A.M., Andermann, M.L., Hood, G., Wetzel, A.W., Yurgenson,
1039 S., Soucy, E.R., Kim, H.S., and Reid, R.C. (2011). Network anatomy and in vivo physiology of
1040 visual cortical neurons. Nature *471*, 177–182. https://doi.org/10.1038/nature09802.

1041 14. Taniguchi, H., He, M., Wu, P., Kim, S., Paik, R., Sugino, K., Kvitsani, D., Fu, Y., Lu, J., Lin, Y., et
1042 al. (2011). A Resource of Cre Driver Lines for Genetic Targeting of GABAergic Neurons in
1043 Cerebral Cortex. Neuron *71*, 995–1013. https://doi.org/10.1016/j.neuron.2011.07.026.

1044 15. Vormstein-Schneider, D., Lin, J.D., Pelkey, K.A., Chittajallu, R., Guo, B., Arias-Garcia, M.A.,
1045 Allaway, K., Sakopoulos, S., Schneider, G., Stevenson, O., et al. (2020). Viral manipulation
1046 of functionally distinct interneurons in mice, non-human primates and humans. Nat
1047 Neurosci *23*, 1629–1636. https://doi.org/10.1038/s41593-020-0692-9.

1048 16. O'Toole, S.M., Oyibo, H.K., and Keller, G.B. (2023). Molecularly targetable cell types in
1049 mouse visual cortex have distinguishable prediction error responses. Neuron *111*, 2918-
1050 2928.e8. https://doi.org/10.1016/j.neuron.2023.08.015.

1051 17. Condylis, C., Ghanbari, A., Manjrekar, N., Bistrong, K., Yao, S., Yao, Z., Nguyen, T.N., Zeng,
1052 H., Tasic, B., and Chen, J.L. (2022). Dense functional and molecular readout of a circuit hub
1053 in sensory cortex. Science *375*, eabl5981. https://doi.org/10.1126/science.abl5981.

1054 18. Bugeon, S., Duffield, J., Dipoppa, M., Ritoux, A., Prankerd, I., Nicoloutsopoulos, D., Orme, D.,
1055 Shinn, M., Peng, H., Forrest, H., et al. (2022). A transcriptomic axis predicts state
1056 modulation of cortical interneurons. Nature *607*, 330–338.
1057 https://doi.org/10.1038/s41586-022-04915-7.

1058 19. Geiller, T., Vancura, B., Terada, S., Troullinou, E., Chavlis, S., Tsagkatakis, G., Tsakalides, P.,
1059 Ócsai, K., Poirazi, P., Rózsa, B.J., et al. (2020). Large-Scale 3D Two-Photon Imaging of
1060 Molecularly Identified CA1 Interneuron Dynamics in Behaving Mice. Neuron *108*, 968-
1061 983.e9. https://doi.org/10.1016/j.neuron.2020.09.013.

1062 20. Vancura, B., Geiller, T., Grosmark, A., Zhao, V., and Losonczy, A. (2023). Inhibitory control of
1063 sharp-wave ripple duration during learning in hippocampal recurrent networks. Nat
1064 Neurosci, 1–10. https://doi.org/10.1038/s41593-023-01306-7.

1065 21. Cohen-Kashi Malina, K., Tsivourakis, E., Kushinsky, D., Apelblat, D., Shtiglitz, S., Zohar, E.,
1066 Sokoletsky, M., Tasaka, G., Mizrahi, A., Lampl, I., et al. (2021). NDNF interneurons in layer

1 gain-modulate whole cortical columns according to an animal's behavioral state. Neuron *109*, 2150-2164.e5. https://doi.org/10.1016/j.neuron.2021.05.001.

22. Hansel, D., and Vreeswijk, C. van (2012). The Mechanism of Orientation Selectivity in Primary Visual Cortex without a Functional Map. J. Neurosci. *32*, 4049–4064. https://doi.org/10.1523/JNEUROSCI.6284-11.2012.

23. Hirokawa, J., Vaughan, A., Masset, P., Ott, T., and Kepecs, A. (2019). Frontal cortex neuron types categorically encode single decision variables. Nature *576*, 446–451. https://doi.org/10.1038/s41586-019-1816-9.

24. Mancinelli, S., and Lodato, S. (2018). Decoding neuronal diversity in the developing cerebral cortex: from single cells to functional networks. Current Opinion in Neurobiology *53*, 146–155. https://doi.org/10.1016/j.conb.2018.08.001.

25. Ohki, K., and Reid, R.C. (2007). Specificity and randomness in the visual cortex. Current Opinion in Neurobiology *17*, 401–407. https://doi.org/10.1016/j.conb.2007.07.007.

26. Peng, H., Xie, P., Liu, L., Kuang, X., Wang, Y., Qu, L., Gong, H., Jiang, S., Li, A., Ruan, Z., et al. (2021). Morphological diversity of single neurons in molecularly defined cell types. Nature *598*, 174–181. https://doi.org/10.1038/s41586-021-03941-1.

27. Treves, A., and Rolls, E.T. (1994). Computational analysis of the role of the hippocampus in memory. Hippocampus *4*, 374–391. https://doi.org/10.1002/hipo.450040319.

28. Buzsáki, G., and Mizuseki, K. (2014). The log-dynamic brain: how skewed distributions affect network operations. Nat Rev Neurosci *15*, 264–278. https://doi.org/10.1038/nrn3687.

29. Cembrowski, M.S., Bachman, J.L., Wang, L., Sugino, K., Shields, B.C., and Spruston, N. (2016). Spatial Gene-Expression Gradients Underlie Prominent Heterogeneity of CA1 Pyramidal Neurons. Neuron *89*, 351–368. https://doi.org/10.1016/j.neuron.2015.12.013.

30. Mallory, C.S., and Giocomo, L.M. (2018). Heterogeneity in hippocampal place coding. Current Opinion in Neurobiology *49*, 158–167. https://doi.org/10.1016/j.conb.2018.02.014.

31. Pettit, N.L., Yap, E.-L., Greenberg, M.E., and Harvey, C.D. (2022). Fos ensembles encode and shape stable spatial maps in the hippocampus. Nature *609*, 327–334. https://doi.org/10.1038/s41586-022-05113-1.

32. Soltesz, I., and Losonczy, A. (2018). CA1 pyramidal cell diversity enabling parallel information processing in the hippocampus. Nat Neurosci *21*, 484–493. https://doi.org/10.1038/s41593-018-0118-0.

33. Sosa, M., Gillespie, A.K., and Frank, L.M. (2018). Neural Activity Patterns Underlying Spatial Coding in the Hippocampus. In Behavioral Neuroscience of Learning and Memory, R. E.

1101 Clark and S. J. Martin, eds. (Springer International Publishing), pp. 43–100.
1102 https://doi.org/10.1007/7854_2016_462.

1103 34. Tanaka, K.Z., He, H., Tomar, A., Niisato, K., Huang, A.J.Y., and McHugh, T.J. (2018). The
1104 hippocampal engram maps experience but not place. Science *361*, 392–397.
1105 https://doi.org/10.1126/science.aat5397.

1106 35. Ziv, Y., Burns, L.D., Cocker, E.D., Hamel, E.O., Ghosh, K.K., Kitch, L.J., Gamal, A.E., and
1107 Schnitzer, M.J. (2013). Long-term dynamics of CA1 hippocampal place codes. Nat Neurosci
1108 *16*, 264–266. https://doi.org/10.1038/nn.3329.

1109 36. Lee, J.S., Briguglio, J.J., Cohen, J.D., Romani, S., and Lee, A.K. (2020). The Statistical Structure
1110 of the Hippocampal Code for Space as a Function of Time, Context, and Value. Cell *183*,
1111 620-635.e22. https://doi.org/10.1016/j.cell.2020.09.024.

1112 37. Kentros, C.G., Agnihotri, N.T., Streater, S., Hawkins, R.D., and Kandel, E.R. (2004). Increased
1113 Attention to Spatial Context Increases Both Place Field Stability and Spatial Memory.
1114 Neuron *42*, 283–295. https://doi.org/10.1016/S0896-6273(04)00192-8.

1115 38. Grosmark, A.D., Sparks, F.T., Davis, M.J., and Losonczy, A. (2021). Reactivation predicts the
1116 consolidation of unbiased long-term cognitive maps. Nat Neurosci *24*, 1574–1585.
1117 https://doi.org/10.1038/s41593-021-00920-7.

1118 39. Keinath, A.T., Mosser, C.-A., and Brandon, M.P. (2022). The representation of context in
1119 mouse hippocampus is preserved despite neural drift. Nat Commun *13*, 2415.
1120 https://doi.org/10.1038/s41467-022-30198-7.

1121 40. Colgin, L.L., Moser, E.I., and Moser, M.-B. (2008). Understanding memory through
1122 hippocampal remapping. Trends in Neurosciences *31*, 469–477.
1123 https://doi.org/10.1016/j.tins.2008.06.008.

1124 41. Moeyaert, B., Holt, G., Madangopal, R., Perez-Alvarez, A., Fearey, B.C., Trojanowski, N.F.,
1125 Ledderose, J., Zolnik, T.A., Das, A., Patel, D., et al. (2018). Improved methods for marking
1126 active neuron populations. Nat Commun *9*, 4440. https://doi.org/10.1038/s41467-018-
1127 06935-2.

1128 42. Hyun, J.H., Nagahama, K., Namkung, H., Mignocchi, N., Roh, S.-E., Hannan, P., Krüssel, S.,
1129 Kwak, C., McElroy, A., Liu, B., et al. (2022). Tagging active neurons by soma-targeted Cal-
1130 Light. Nat Commun *13*, 7692. https://doi.org/10.1038/s41467-022-35406-y.

1131 43. Mocle, A.J., Ramsaran, A.I., Jacob, A.D., Rashid, A.J., Luchetti, A., Tran, L.M., Richards, B.A.,
1132 Frankland, P.W., and Josselyn, S.A. (2024). Excitability mediates allocation of pre-
1133 configured ensembles to a hippocampal engram supporting contextual conditioned threat
1134 in mice. Neuron *112*, 1487-1497.e6. https://doi.org/10.1016/j.neuron.2024.02.007.

1135 44. DeNardo, L.A., Liu, C.D., Allen, W.E., Adams, E.L., Friedmann, D., Fu, L., Guenthner, C.J.,
1136 Tessier-Lavigne, M., and Luo, L. (2019). Temporal evolution of cortical ensembles
1137 promoting remote memory retrieval. Nat Neurosci *22*, 460–469.
1138 https://doi.org/10.1038/s41593-018-0318-7.

1139 45. Guenthner, C.J., Miyamichi, K., Yang, H.H., Heller, H.C., and Luo, L. (2013). Permanent
1140 Genetic Access to Transiently Active Neurons via TRAP: Targeted Recombination in Active
1141 Populations. Neuron *78*, 773–784. https://doi.org/10.1016/j.neuron.2013.03.025.

1142 46. Lee, D., Hyun, J.H., Jung, K., Hannan, P., and Kwon, H.-B. (2017). A calcium- and light-gated
1143 switch to induce gene expression in activated neurons. Nat Biotechnol *35*, 858–863.
1144 https://doi.org/10.1038/nbt.3902.

1145 47. Sørensen, A.T., Cooper, Y.A., Baratta, M.V., Weng, F.-J., Zhang, Y., Ramamoorthi, K., Fropf,
1146 R., LaVerriere, E., Xue, J., Young, A., et al. (2016). A robust activity marking system for
1147 exploring active neuronal ensembles. eLife *5*, e13918.
1148 https://doi.org/10.7554/eLife.13918.

1149 48. Datta, S.R., Vasconcelos, M.L., Ruta, V., Luo, S., Wong, A., Demir, E., Flores, J., Balonze, K.,
1150 Dickson, B.J., and Axel, R. (2008). The Drosophila pheromone cVA activates a sexually
1151 dimorphic neural circuit. Nature *452*, 473–477. https://doi.org/10.1038/nature06808.

1152 49. Lien, A.D., and Scanziani, M. (2011). In vivo Labeling of Constellations of Functionally
1153 Identified Neurons for Targeted in vitro Recordings. Front Neural Circuits *5*, 16.
1154 https://doi.org/10.3389/fncir.2011.00016.

1155 50. Lee, D., Kume, M., and Holy, T.E. (2019). Sensory coding mechanisms revealed by optical
1156 tagging of physiologically defined neuronal types. Science *366*, 1384–1389.
1157 https://doi.org/10.1126/science.aax8055.

1158 51. Dana, H., Sun, Y., Mohar, B., Hulse, B.K., Kerlin, A.M., Hasseman, J.P., Tsegaye, G., Tsang, A.,
1159 Wong, A., Patel, R., et al. (2019). High-performance calcium sensors for imaging activity in
1160 neuronal populations and microcompartments. Nat Methods *16*, 649–657.
1161 https://doi.org/10.1038/s41592-019-0435-6.

1162 52. Scheyltjens, I., Laramée, M.-E., Van den Haute, C., Gijsbers, R., Debyser, Z., Baekelandt, V.,
1163 Vreysen, S., and Arckens, L. (2015). Evaluation of the expression pattern of rAAV2/1, 2/5,
1164 2/7, 2/8, and 2/9 serotypes with different promoters in the mouse visual cortex. Journal of
1165 Comparative Neurology *523*, 2019–2042. https://doi.org/10.1002/cne.23819.

1166 53. Geiller, T., Priestley, J.B., and Losonczy, A. (2023). A local circuit-basis for spatial navigation
1167 and memory processes in hippocampal area CA1. Current Opinion in Neurobiology *79*,
1168 102701. https://doi.org/10.1016/j.conb.2023.102701.

1169 54. Katona, G., Szalay, G., Maák, P., Kaszás, A., Veress, M., Hillier, D., Chiovini, B., Vizi, E.S.,
1170 Roska, B., and Rózsa, B. (2012). Fast two-photon in vivo imaging with three-dimensional

1171 random-access scanning in large tissue volumes. Nat Methods *9*, 201–208.
1172 https://doi.org/10.1038/nmeth.1851.

1173 55. Apelblat, D., Roethler, O., Bitan, L., Keren-Shaul, H., and Spiegel, I. (2022). Meso-seq for in-
1174 depth transcriptomics in ultra-low amounts of FACS-purified neuronal nuclei. Cell Reports
1175 Methods *2*, 100259. https://doi.org/10.1016/j.crmeth.2022.100259.

1176 56. Roethler, O., Zohar, E., Cohen-Kashi Malina, K., Bitan, L., Gabel, H.W., and Spiegel, I. (2023).
1177 Single genomic enhancers drive experience-dependent GABAergic plasticity to maintain
1178 sensory processing in the adult cortex. Neuron *111*, 2693-2708.e8.
1179 https://doi.org/10.1016/j.neuron.2023.05.026.

1180 57. O'Keefe, J., and Dostrovsky, J. (1971). The hippocampus as a spatial map. Preliminary
1181 evidence from unit activity in the freely-moving rat. Brain Research *34*, 171–175.
1182 https://doi.org/10.1016/0006-8993(71)90358-1.

1183 58. Witharana, W. k. l., Cardiff, J., Chawla, M. k., Xie, J. y., Alme, C. b., Eckert, M., Lapointe, V.,
1184 Demchuk, A., Maurer, A. p., Trivedi, V., et al. (2016). Nonuniform allocation of
1185 hippocampal neurons to place fields across all hippocampal subfields. Hippocampus *26*,
1186 1328–1344. https://doi.org/10.1002/hipo.22609.

1187 59. Cembrowski, M.S. (2019). Single-cell transcriptomics as a framework and roadmap for
1188 understanding the brain. Journal of Neuroscience Methods *326*, 108353.
1189 https://doi.org/10.1016/j.jneumeth.2019.108353.

1190 60. Yao, Z., Velthoven, C.T.J. van, Nguyen, T.N., Goldy, J., Sedeno-Cortes, A.E., Baftizadeh, F.,
1191 Bertagnolli, D., Casper, T., Chiang, M., Crichton, K., et al. (2021). A taxonomy of
1192 transcriptomic cell types across the isocortex and hippocampal formation. Cell *184*, 3222-
1193 3241.e26. https://doi.org/10.1016/j.cell.2021.04.021.

1194 61. Rich, P.D., Liaw, H.-P., and Lee, A.K. (2014). Large environments reveal the statistical
1195 structure governing hippocampal representations. Science *345*, 814–817.
1196 https://doi.org/10.1126/science.1255635.

1197 62. Thompson, L.T., and Best, P.J. (1989). Place cells and silent cells in the hippocampus of
1198 freely-behaving rats. J. Neurosci. *9*, 2382–2390. https://doi.org/10.1523/JNEUROSCI.09-
1199 07-02382.1989.

1200 63. Wilson, M.A., and McNaughton, B.L. (1993). Dynamics of the Hippocampal Ensemble Code
1201 for Space. Science *261*, 1055–1058. https://doi.org/10.1126/science.8351520.

1202 64. Zaremba, J.D., Diamantopoulou, A., Danielson, N.B., Grosmark, A.D., Kaifosh, P.W., Bowler,
1203 J.C., Liao, Z., Sparks, F.T., Gogos, J.A., and Losonczy, A. (2017). Impaired hippocampal place
1204 cell dynamics in a mouse model of the 22q11.2 deletion. Nat Neurosci *20*, 1612–1623.
1205 https://doi.org/10.1038/nn.4634.

1206 65. Bowler, J.C., and Losonczy, A. (2023). Direct cortical inputs to hippocampal area CA1
1207 transmit complementary signals for goal-directed navigation. Neuron *0*.
1208 https://doi.org/10.1016/j.neuron.2023.09.013.

1209 66. Bowler, J.C., Zakka, G., Yong, H.C., Li, W., Rao, B., Liao, Z., Priestley, J.B., and Losonczy, A.
1210 (2024). behaviorMate: An Intranet of Things Approach for Adaptable Control
1211 of Behavioral and Navigation-Based Experiments. bioRxiv, 2023.12.04.569989.
1212 https://doi.org/10.1101/2023.12.04.569989.

1213 67. Priestley, J.B., Bowler, J.C., Rolotti, S.V., Fusi, S., and Losonczy, A. (2022). Signatures of rapid
1214 plasticity in hippocampal CA1 representations during novel experiences. Neuron,
1215 S0896627322002628. https://doi.org/10.1016/j.neuron.2022.03.026.

1216 68. Rolotti, S.V., Ahmed, M.S., Szoboszlay, M., Geiller, T., Negrean, A., Blockus, H., Gonzalez,
1217 K.C., Sparks, F.T., Solis Canales, A.S., Tuttman, A.L., et al. (2022). Local feedback inhibition
1218 tightly controls rapid formation of hippocampal place fields. Neuron *110*, 783-794.e6.
1219 https://doi.org/10.1016/j.neuron.2021.12.003.

1220 69. Geiller, T., Sadeh, S., Rolotti, S.V., Blockus, H., Vancura, B., Negrean, A., Murray, A.J., Rózsa,
1221 B., Polleux, F., Clopath, C., et al. (2022). Local circuit amplification of spatial selectivity in
1222 the hippocampus. Nature *601*, 105–109. https://doi.org/10.1038/s41586-021-04169-9.

1223 70. Jeon, B.B., Swain, A.D., Good, J.T., Chase, S.M., and Kuhlman, S.J. (2018). Feature selectivity
1224 is stable in primary visual cortex across a range of spatial frequencies. Sci Rep *8*, 15288.
1225 https://doi.org/10.1038/s41598-018-33633-2.

1226 71. Cembrowski, M.S., Wang, L., Sugino, K., Shields, B.C., and Spruston, N. (2016). Hipposeq: a
1227 comprehensive RNA-seq database of gene expression in hippocampal principal neurons.
1228 eLife *5*, e14997. https://doi.org/10.7554/eLife.14997.

1229 72. Bloodgood, B.L., Sharma, N., Browne, H.A., Trepman, A.Z., and Greenberg, M.E. (2013). The
1230 activity-dependent transcription factor NPAS4 regulates domain-specific inhibition. Nature
1231 *503*, 121–125. https://doi.org/10.1038/nature12743.

1232 73. Sheng, M., and Greenberg, M.E. (1990). The regulation and function of c-*fos* and other
1233 immediate early genes in the nervous system. Neuron *4*, 477–485.
1234 https://doi.org/10.1016/0896-6273(90)90106-P.

1235 74. Spiegel, I., Mardinly, A.R., Gabel, H.W., Bazinet, J.E., Couch, C.H., Tzeng, C.P., Harmin, D.A.,
1236 and Greenberg, M.E. (2014). Npas4 Regulates Excitatory-Inhibitory Balance within Neural
1237 Circuits through Cell-Type-Specific Gene Programs. Cell *157*, 1216–1229.
1238 https://doi.org/10.1016/j.cell.2014.03.058.

1239 75. Apoptosis: A Review of Programmed Cell Death - Susan Elmore, 2007
1240 https://journals.sagepub.com/doi/10.1080/01926230701320337.

1241 76. Xu, J., Burgoyne, P.S., and Arnold, A.P. (2002). Sex differences in sex chromosome gene
1242 expression in mouse brain. Human Molecular Genetics *11*, 1409–1419.
1243 https://doi.org/10.1093/hmg/11.12.1409.

1244 77. Nichols, C.G., and Lopatin, A.N. (1997). INWARD RECTIFIER POTASSIUM CHANNELS. Annual
1245 Review of Physiology *59*, 171–191. https://doi.org/10.1146/annurev.physiol.59.1.171.

1246 78. Reimann, F., and Ashcroft, F.M. (1999). Inwardly rectifying potassium channels. Current
1247 Opinion in Cell Biology *11*, 503–508. https://doi.org/10.1016/S0955-0674(99)80073-8.

1248 79. Shcherbatyy, V., Carson, J., Yaylaoglu, M., Jäckle, K., Grabbe, F., Brockmeyer, M., Yavuz, H.,
1249 and Eichele, G. (2015). A Digital Atlas of Ion Channel Expression Patterns in the Two-Week-
1250 Old Rat Brain. Neuroinform *13*, 111–125. https://doi.org/10.1007/s12021-014-9247-0.

1251 80. Alkon, D.L., Epstein, H., Kuzirian, A., Bennett, M.C., and Nelson, T.J. (2005). Protein synthesis
1252 required for long-term memory is induced by PKC activation on days before associative
1253 learning. Proceedings of the National Academy of Sciences *102*, 16432–16437.
1254 https://doi.org/10.1073/pnas.0508001102.

1255 81. Gottschall, P.E., and Howell, M.D. (2015). ADAMTS expression and function in central
1256 nervous system injury and disorders. Matrix Biology *44–46*, 70–76.
1257 https://doi.org/10.1016/j.matbio.2015.01.014.

1258 82. Epsztein, J., Brecht, M., and Lee, A.K. (2011). Intracellular Determinants of Hippocampal
1259 CA1 Place and Silent Cell Activity in a Novel Environment. Neuron *70*, 109–120.
1260 https://doi.org/10.1016/j.neuron.2011.03.006.

1261 83. Santoni, G., Astori, S., Leleu, M., Glauser, L., Zamora, S.A., Schioppa, M., Tarulli, I., Sandi, C.,
1262 and Gräff, J. (2024). Chromatin plasticity predetermines neuronal eligibility for memory
1263 trace formation. Science *385*, eadg9982. https://doi.org/10.1126/science.adg9982.

1264 84. Yiu, A.P., Mercaldo, V., Yan, C., Richards, B., Rashid, A.J., Hsiang, H.-L.L., Pressey, J.,
1265 Mahadevan, V., Tran, M.M., Kushner, S.A., et al. (2014). Neurons Are Recruited to a
1266 Memory Trace Based on Relative Neuronal Excitability Immediately before Training.
1267 Neuron *83*, 722–735. https://doi.org/10.1016/j.neuron.2014.07.017.

1268 85. Josselyn, S.A., and Frankland, P.W. (2018). Memory Allocation: Mechanisms and Function.
1269 Annual Review of Neuroscience *41*, 389–413. https://doi.org/10.1146/annurev-neuro-
1270 080317-061956.

1271 86. Sano, Y., Shobe, J.L., Zhou, M., Huang, S., Shuman, T., Cai, D.J., Golshani, P., Kamata, M., and
1272 Silva, A.J. (2014). CREB Regulates Memory Allocation in the Insular Cortex. Current Biology
1273 *24*, 2833–2837. https://doi.org/10.1016/j.cub.2014.10.018.

87. Mizuseki, K., and Buzsáki, G. (2013). Preconfigured, Skewed Distribution of Firing Rates in the Hippocampus and Entorhinal Cortex. Cell Reports *4*, 1010–1021. https://doi.org/10.1016/j.celrep.2013.07.039.

88. Alme, C.B., Miao, C., Jezek, K., Treves, A., Moser, E.I., and Moser, M.-B. (2014). Place cells in the hippocampus: Eleven maps for eleven rooms. Proceedings of the National Academy of Sciences *111*, 18428–18435. https://doi.org/10.1073/pnas.1421056111.

89. Dragoi, G., and Tonegawa, S. (2011). Preplay of future place cell sequences by hippocampal cellular assemblies. Nature *469*, 397–401. https://doi.org/10.1038/nature09633.

90. Dragoi, G., and Tonegawa, S. (2014). Selection of preconfigured cell assemblies for representation of novel spatial experiences. Philosophical Transactions of the Royal Society B: Biological Sciences *369*, 20120522. https://doi.org/10.1098/rstb.2012.0522.

91. Grosmark, A.D., and Buzsáki, G. (2016). Diversity in neural firing dynamics supports both rigid and learned hippocampal sequences. Science *351*, 1440–1443. https://doi.org/10.1126/science.aad1935.

92. Huszár, R., Zhang, Y., Blockus, H., and Buzsáki, G. (2022). Preconfigured dynamics in the hippocampus are guided by embryonic birthdate and rate of neurogenesis. Nat Neurosci *25*, 1201–1212. https://doi.org/10.1038/s41593-022-01138-x.

93. Cossart, R., and Khazipov, R. (2022). How development sculpts hippocampal circuits and function. Physiological Reviews *102*, 343–378. https://doi.org/10.1152/physrev.00044.2020.

94. Donato, F., Jacobsen, R.I., Moser, M.-B., and Moser, E.I. (2017). Stellate cells drive maturation of the entorhinal-hippocampal circuit. Science *355*, eaai8178. https://doi.org/10.1126/science.aai8178.

95. Deguchi, Y., Donato, F., Galimberti, I., Cabuy, E., and Caroni, P. (2011). Temporally matched subpopulations of selectively interconnected principal neurons in the hippocampus. Nat Neurosci *14*, 495–504. https://doi.org/10.1038/nn.2768.

96. Kveim, V.A., Salm, L., Ulmer, T., Lahr, M., Kandler, S., Imhof, F., and Donato, F. (2024). Divergent recruitment of developmentally defined neuronal ensembles supports memory dynamics. Science *385*, eadk0997. https://doi.org/10.1126/science.adk0997.

97. Marissal, T., Bonifazi, P., Picardo, M.A., Nardou, R., Petit, L.F., Baude, A., Fishell, G.J., Ben-Ari, Y., and Cossart, R. (2012). Pioneer glutamatergic cells develop into a morpho-functionally distinct population in the juvenile CA3 hippocampus. Nat Commun *3*, 1316. https://doi.org/10.1038/ncomms2318.

98. Jovasevic, V., Wood, E.M., Cicvaric, A., Zhang, H., Petrovic, Z., Carboncino, A., Parker, K.K., Bassett, T.E., Moltesen, M., Yamawaki, N., et al. (2024). Formation of memory assemblies

through the DNA-sensing TLR9 pathway. Nature *628*, 145–153. https://doi.org/10.1038/s41586-024-07220-7.

99. Solstad, T., Boccara, C.N., Kropff, E., Moser, M.-B., and Moser, E.I. (2008). Representation of Geometric Borders in the Entorhinal Cortex. Science *322*, 1865–1868. https://doi.org/10.1126/science.1166466.

100. Taube, J.S., Muller, R.U., and Ranck, J.B. (1990). Head-direction cells recorded from the postsubiculum in freely moving rats. I. Description and quantitative analysis. J. Neurosci. *10*, 420–435. https://doi.org/10.1523/JNEUROSCI.10-02-00420.1990.

101. Eichenbaum, H. (2014). Time cells in the hippocampus: a new dimension for mapping memories. Nat Rev Neurosci *15*, 732–744. https://doi.org/10.1038/nrn3827.

102. Driscoll, L.N., Duncker, L., and Harvey, C.D. (2022). Representational drift: Emerging theories for continual learning and experimental future directions. Current Opinion in Neurobiology *76*, 102609. https://doi.org/10.1016/j.conb.2022.102609.

103. Josselyn, S.A., and Tonegawa, S. (2020). Memory engrams: Recalling the past and imagining the future. Science *367*, eaaw4325. https://doi.org/10.1126/science.aaw4325.

104. Xu, S., Yang, H., Menon, V., Lemire, A.L., Wang, L., Henry, F.E., Turaga, S.C., and Sternson, S.M. (2020). Behavioral state coding by molecularly defined paraventricular hypothalamic cell type ensembles. Science *370*, eabb2494. https://doi.org/10.1126/science.abb2494.

105. Chen, K.H., Boettiger, A.N., Moffitt, J.R., Wang, S., and Zhuang, X. (2015). Spatially resolved, highly multiplexed RNA profiling in single cells. Science *348*, aaa6090. https://doi.org/10.1126/science.aaa6090.

106. Chen, S., Rao, B.Y., Herrlinger, S., Losonczy, A., Paninski, L., and Varol, E. (2023). Multimodal Microscopy Image Alignment Using Spatial and Shape Information and a Branch-and-Bound Algorithm. In ICASSP 2023 - 2023 IEEE International Conference on Acoustics, Speech and Signal Processing (ICASSP), pp. 1–5. https://doi.org/10.1109/ICASSP49357.2023.10096185.

107. Rao, B.Y., Peterson, A.M., Kandror, E.K., Herrlinger, S., Losonczy, A., Paninski, L., Rizvi, A.H., and Varol, E. (2021). Non-parametric Vignetting Correction for Sparse Spatial Transcriptomics Images. In Medical Image Computing and Computer Assisted Intervention – MICCAI 2021, M. de Bruijne, P. C. Cattin, S. Cotin, N. Padoy, S. Speidel, Y. Zheng, and C. Essert, eds. (Springer International Publishing), pp. 466–475. https://doi.org/10.1007/978-3-030-87237-3_45.

108. Bittner, K.C., Milstein, A.D., Grienberger, C., Romani, S., and Magee, J.C. (2017). Behavioral time scale synaptic plasticity underlies CA1 place fields. Science *357*, 1033–1036. https://doi.org/10.1126/science.aan3846.

1344 109. Magee, J.C., and Grienberger, C. (2020). Synaptic Plasticity Forms and Functions. Annual
1345 Review of Neuroscience *43*, 95–117. https://doi.org/10.1146/annurev-neuro-090919-
1346 022842.

1347 110. Xue, M., Atallah, B.V., and Scanziani, M. (2014). Equalizing excitation–inhibition ratios
1348 across visual cortical neurons. Nature *511*, 596–600.
1349 https://doi.org/10.1038/nature13321.

1350 111. Wright, W.J., Hedrick, N.G., and Komiyama, T. (2025). Distinct synaptic plasticity rules
1351 operate across dendritic compartments in vivo during learning. Science *388*, 322–328.
1352 https://doi.org/10.1126/science.ads4706.

1353 112. Kaifosh, P., Zaremba, J.D., Danielson, N.B., and Losonczy, A. (2014). SIMA: Python software
1354 for analysis of dynamic fluorescence imaging data. Front. Neuroinform. *8*.
1355 https://doi.org/10.3389/fninf.2014.00080.

1356 113. Pachitariu, M., Stringer, C., Dipoppa, M., Schröder, S., Rossi, L.F., Dalgleish, H., Carandini,
1357 M., and Harris, K.D. (2017). Suite2p: beyond 10,000 neurons with standard two-photon
1358 microscopy. bioRxiv, 061507. https://doi.org/10.1101/061507.

1359 114. Stringer, C., Wang, T., Michaelos, M., and Pachitariu, M. (2021). Cellpose: a generalist
1360 algorithm for cellular segmentation. Nat Methods *18*, 100–106.
1361 https://doi.org/10.1038/s41592-020-01018-x.

1362 115. Muzellec, B., Teleńczuk, M., Cabeli, V., and Andreux, M. (2023). PyDESeq2: a python
1363 package for bulk RNA-seq differential expression analysis. Bioinformatics *39*, btad547.
1364 https://doi.org/10.1093/bioinformatics/btad547.

1365 116. Friedrich, J., Zhou, P., and Paninski, L. (2017). Fast online deconvolution of calcium imaging
1366 data. PLOS Computational Biology *13*, e1005423.
1367 https://doi.org/10.1371/journal.pcbi.1005423.

1368 117. O'Hare, J.K., Gonzalez, K.C., Herrlinger, S.A., Hirabayashi, Y., Hewitt, V.L., Blockus, H.,
1369 Szoboszlay, M., Rolotti, S.V., Geiller, T.C., Negrean, A., et al. (2022). Compartment-specific
1370 tuning of dendritic feature selectivity by intracellular Ca2+ release. Science *375*,
1371 eabm1670. https://doi.org/10.1126/science.abm1670.

1372 118. Münch, B., Trtik, P., Marone, F., and Stampanoni, M. (2009). Stripe and ring artifact
1373 removal with combined wavelet — Fourier filtering. Opt. Express, OE *17*, 8567–8591.
1374 https://doi.org/10.1364/OE.17.008567.

1375 119. Schindelin, J., Arganda-Carreras, I., Frise, E., Kaynig, V., Longair, M., Pietzsch, T., Preibisch,
1376 S., Rueden, C., Saalfeld, S., Schmid, B., et al. (2012). Fiji: an open-source platform for
1377 biological-image analysis. Nature Methods *9*, 676–682.
1378 https://doi.org/10.1038/nmeth.2019.

1379 120. Dobin, A., Davis, C.A., Schlesinger, F., Drenkow, J., Zaleski, C., Jha, S., Batut, P., Chaisson,
1380 M., and Gingeras, T.R. (2013). STAR: ultrafast universal RNA-seq aligner. Bioinformatics *29*,
1381 15–21. https://doi.org/10.1093/bioinformatics/bts635.

1382 121. Anders, S., Pyl, P.T., and Huber, W. (2015). HTSeq—a Python framework to work with high-
1383 throughput sequencing data. Bioinformatics *31*, 166–169.
1384 https://doi.org/10.1093/bioinformatics/btu638.

1385 122. Fang, Z., Liu, X., and Peltz, G. (2023). GSEApy: a comprehensive package for performing
1386 gene set enrichment analysis in Python. Bioinformatics *39*, btac757.
1387 https://doi.org/10.1093/bioinformatics/btac757.

Supplementary Figures

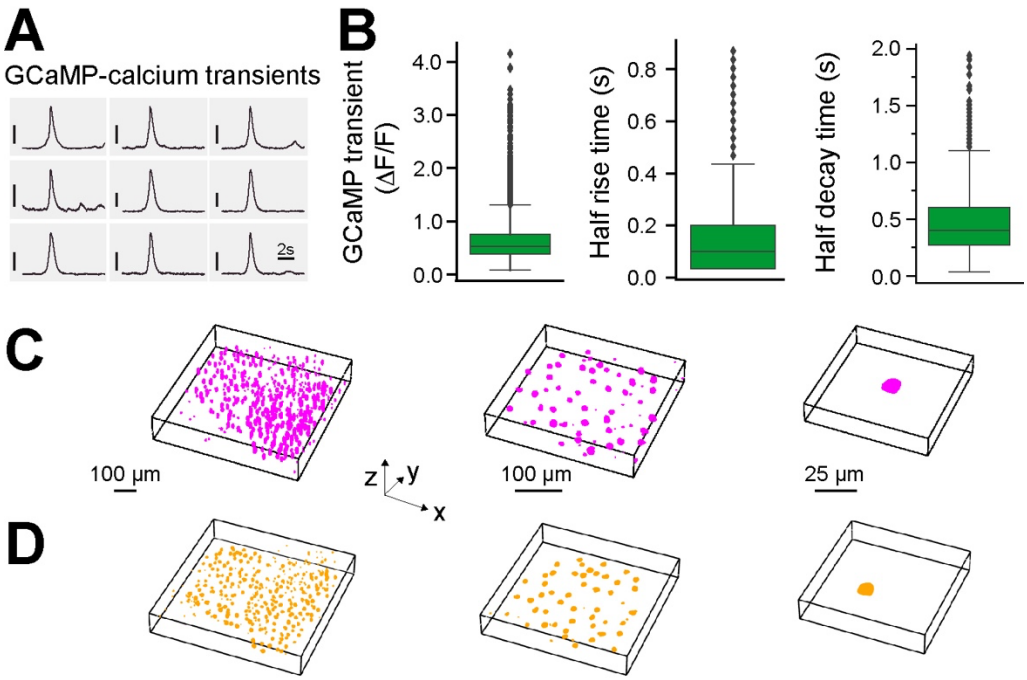

Figure S1. Additional data on 2P-NucTag. (**A**) Representative average GCaMP-Ca^{2+} transients from nine CA1 PNs, vertical scale bar (50% ΔF/F). (**B**) Left: GCaMP amplitude (54.6% ± 0.3% ΔF/F, n = 8190 cells in 9 mice). Middle: GCaMP half rise time (0.15s ± 0.001s, n = 7797 cells in 9 mice), Right: GCaMP half decay time (0.44s ± 0.003s, n = 8282 cells in 9 mice, 940 nm excitation, See methods for cell exclusion criterion). Boxplots show the 25th, 50th (median), and 75th quartile ranges, with the whiskers extending to 1.5 interquartile ranges below or above the 25th or 75th quartiles, respectively. Outliers are defined as values extending beyond the whisker ranges. (**C**) Left: *in vivo* 3D visualization of the entire field of view (FOV). Middle: subset of *in vivo* 3D visualization. Right: representative cell from *in vivo* 3D visualization. (**D**) Left: *ex vivo* confocal 3D visualization of entire FOV. Middle: subset of *ex vivo* 3D visualization. Right: representative cell from *ex vivo* 3D visualization. *C* and *D* are corresponding to *Figure 1F*.

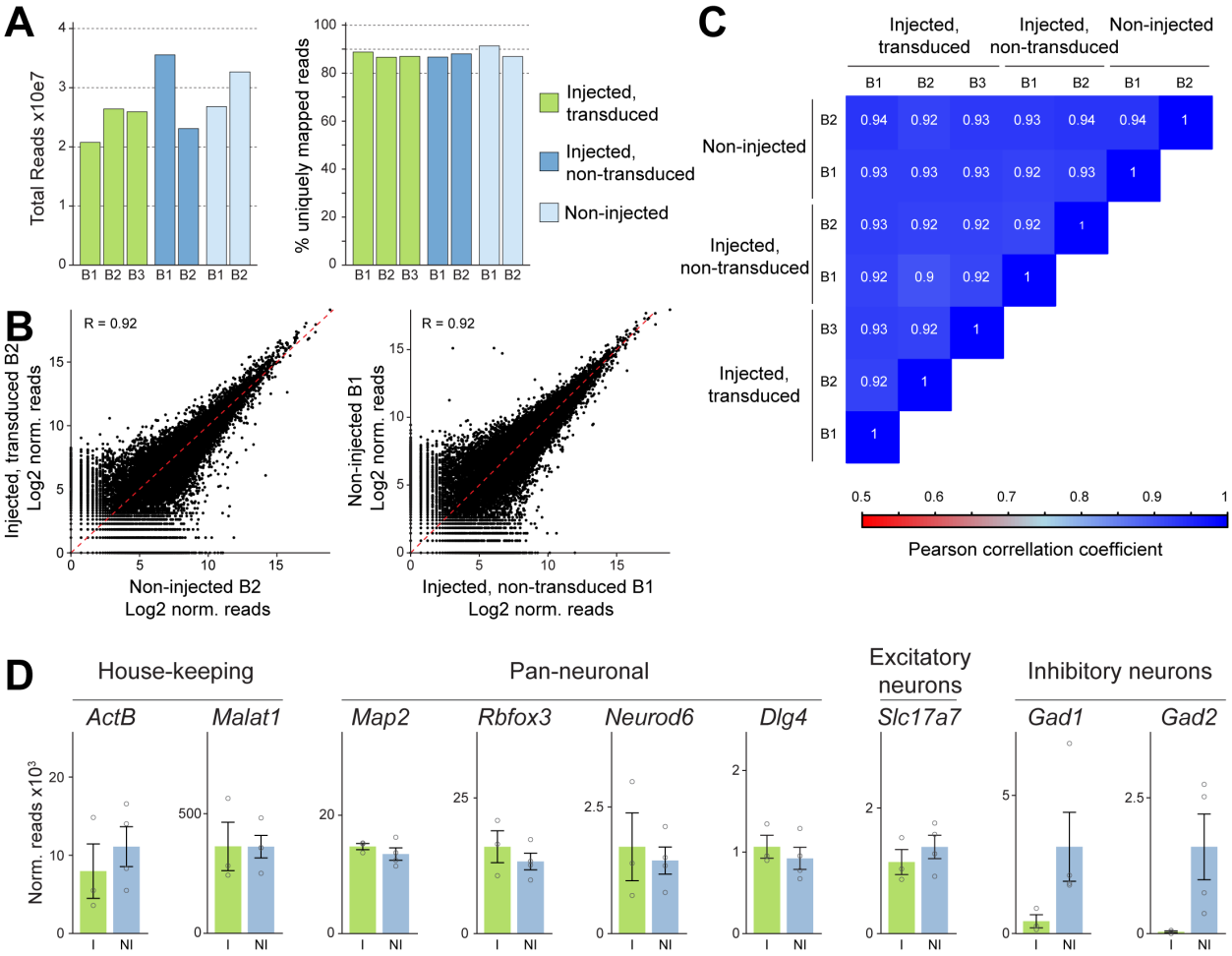

Figure S2. Meso-seq on hippocampal CA1 pyramidal neurons with 2P-NucTag construct. (**A**) Total reads and percentage of uniquely mapped reads from all libraries (B = biological replicate). (**B,C**) Pearson-correlations of all pair-wise comparisons of the expression levels of all expressed genes in the 7 libraries. (**B**) Two example comparisons. (**C**) Correlation coefficients of all comparisons (B = biological replicate). (**D**) Expression values of example genes in non-transduced neurons (NI = pool of "Non-injected" and "Injected, non-tranduced") and transduced neurons (I = "Injected, transduced") (error-bars = SEM).

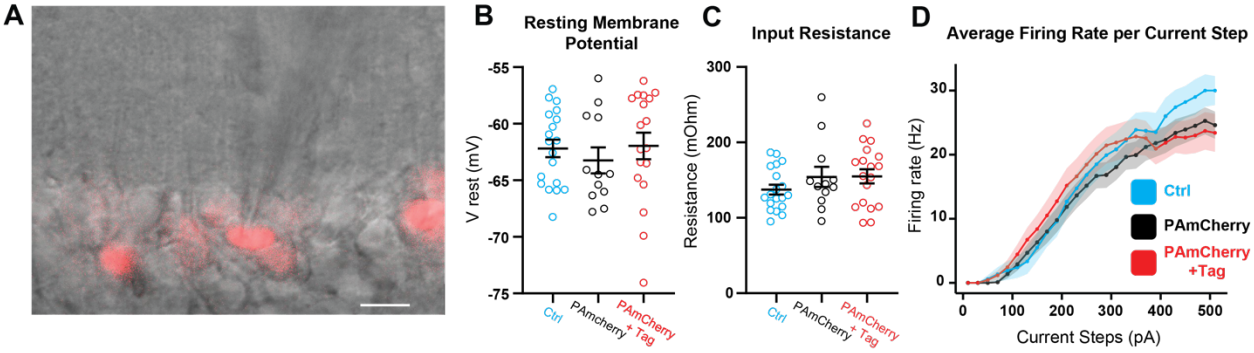

Figure S3. The 2P-NucTag construct does not alter the intrinsic properties of the CA1 pyramidal neurons. (**A**) Representative image of CA1 pyramidal neurons with (red fluorescence) and without photoactivation during whole cell patch clamp recording. Scale bar: 10 µm. (**B,C**) Quantified data of Resting membrane potential and Input resistance in CA1 excitatory neurons. Blue - control neurons (*Ctrl*), recorded in CA1 of the contralateral non-infected hemisphere. Black- are the neurons recorded from the infected hemisphere but have not been phototagged (*PAmCherry*). Red (*PAmCherry+Tag*) are the phototagged neurons (Ctrl n = 19 cells from 7 mice; PAmCherry n = 12 cells from 8 mice; PAmCherry+Tag n = 18 cells from 7 mice; Statistics Kruskal-Wallis test with post-hoc Dunnett's T3 multiple comparisons test: no statistically significant differences were observed). (**D**) Average firing rate per current step (F-I curve) in each condition. (error bars represent SEM in all data panels).

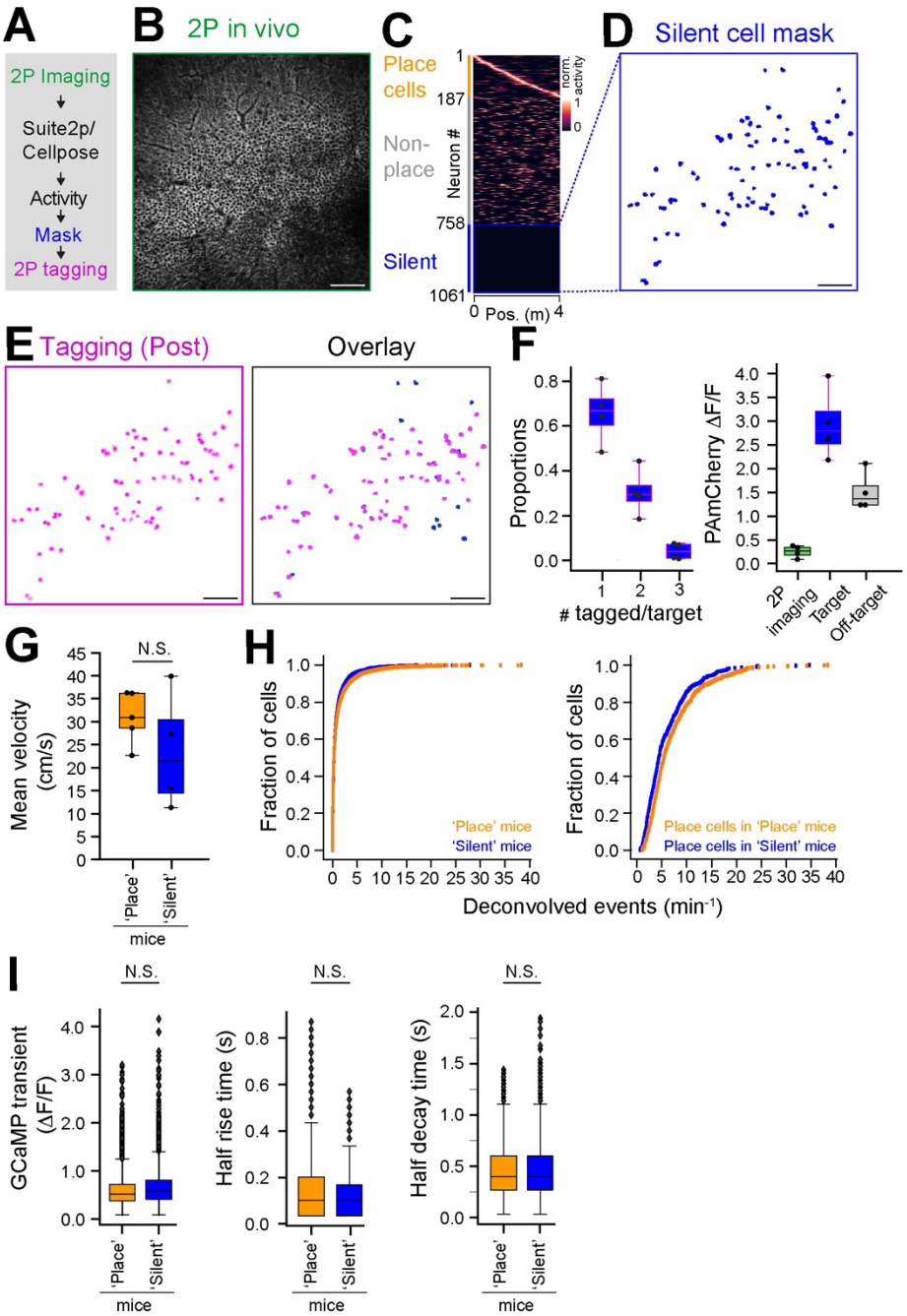

Figure S4. *In vivo* 2P-NucTag of silent cells. (**A**) Pipeline for two-photon (*2P*) phototagging of functionally identified 'silent' neurons in CA1 during VR spatial navigation (as in *Figure 1B*). (**B**) Example 2P imaging field of view (FOV) of GCaMP in the CA1 pyramidal layer from a mouse with "silent" cells targeted. Scale bar: 100 µm. (**C**) CA1PNs detected with Suite2p/Cellpose in the FOV shown in *B*. (**D**) Spatial mask (blue) of identified 'silent' cells from the FOV in *B.* Scale bar: 100 µm. (**E**) Left: PAmCherry fluorescence (magenta) of tagged nuclei after 2P phototagging. Right: overlay of spatial masks of identified CA1PNs and tagged nuclei for the FOVs in *D* and *E.* Note that we only tagged a subset of silent cells present in the FOV. Scale bar: 100 µm. (**F**) Left: Proportion of single, double, and triple-tagged nuclei following phototagging of a single silent cell. Right: relative PAmCherry fluorescence change for non-tagged cells in the FOV after 2P imaging (green), after 2P phototagging of targeted silent cell nuclei (blue) and off-target nuclei (gray, n = 4 mice). (**G**) Average velocity of the mice during virtual reality navigation task (Mann-Whitney U test, p-value = 0.286). (**H**) Left: deconvolved events per minute from all cells across all mice from 2P GCaMP-

Ca^{2+}imaging (averaged across mice, n = 5 'Place' mice, n = 4 'Silent' mice, Mann-Whitney U Test, p-value = 0.28). Right: deconvolved events per minute from place cells across all mice (averaged across mice, place n = 5, silent n = 4, Mann-Whitney U Test, p-value = 0.90). (**I**) Left: GCaMP transient amplitude of all cells between groups (averaged across mice, n = 5 'Place' mice, n = 4 'Silent' mice, Mann-Whitney U Test, p-value = 0.14), Middle: GCaMP half rise time of all cells between groups (averaged across mice, n = 5 'Place' mice, n = 4 'Silent' mice, Mann-Whitney U Test, p-value = 0.14), Right: GCaMP half decay time of all cells between groups (averaged across mice, n = 5 'Place' mice, n = 4 'Silent' mice, Mann-Whitney U Test, p-value = 0.81). Boxplots show the 25th, 50th (median), and 75th quartile ranges, with the whiskers extending to 1.5 interquartile ranges below or above the 25th or 75th quartiles, respectively. Outliers are defined as values extending beyond the whisker ranges.

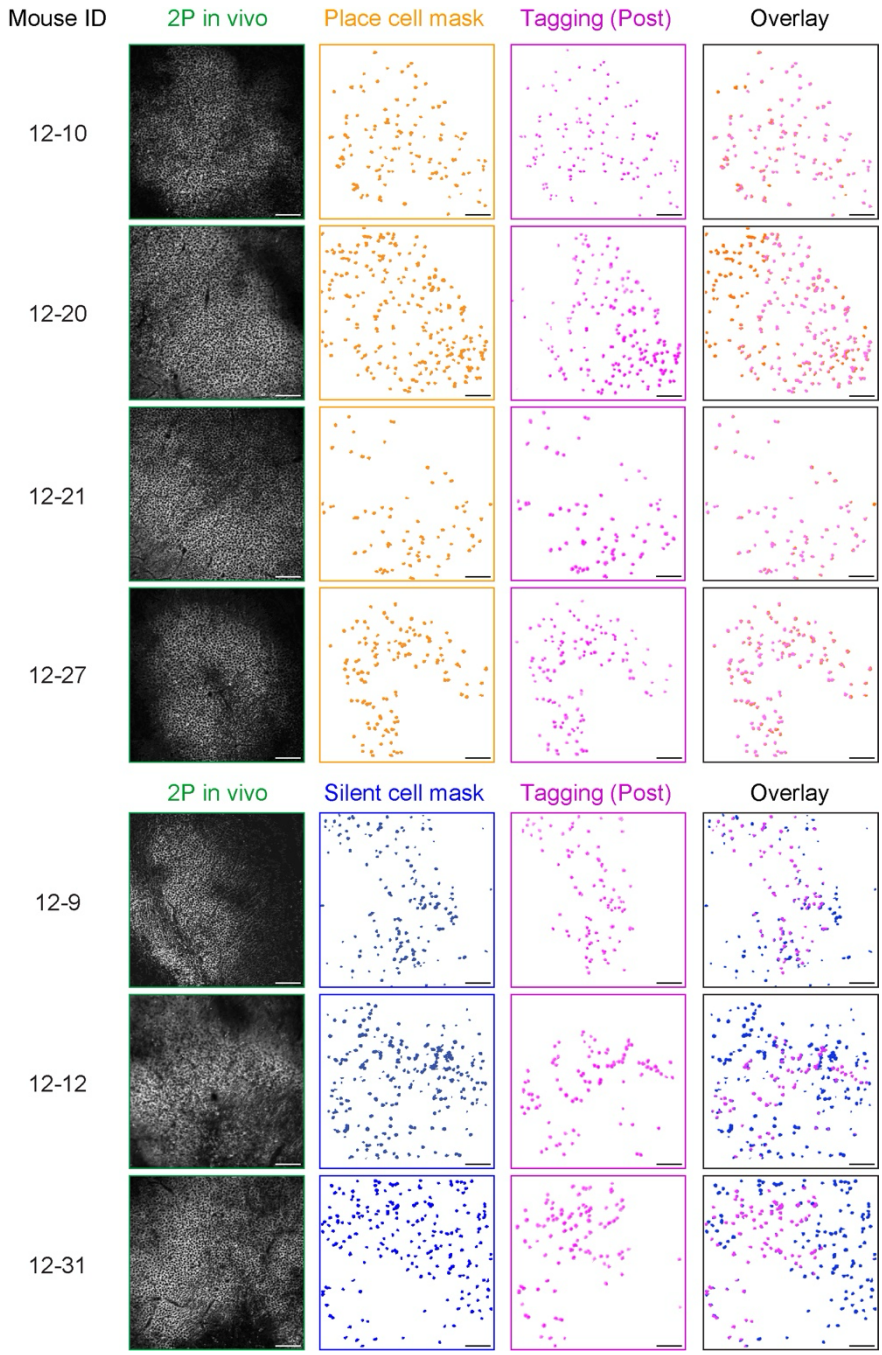

Figure S5. Additional data on phototagging. From left to right by column: animal ID (animals in *Figure 2* and *figure S2* are not shown here), *in vivo* two-photon (*2P*) imaging fields of view (FOVs), functionally defined masks (orange for place cells and blue for silent cells), PAmCherry fluorescence (magenta) of tagged nuclei after 2P phototagging and overlay of spatial masks from identified CA1PNs and tagged nuclei for the respective FOV in the same row. Note that we only tagged a subset of silent cells present in the FOV in 'Silent' mice, in order to approximate the number of phototagged place cells in 'Place' mice. Scale bar: 100 µm.

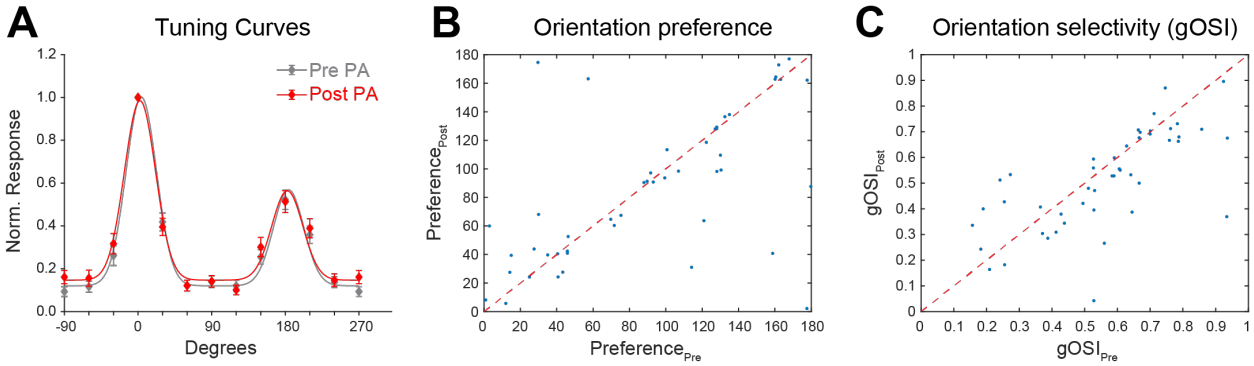

Fig. S6. Orientation tuning of visually responsive neurons in V1 before and after photoactivation. (**A**) tuning curve for visually responsive neurons before and after photoactivation (Gray – before photoactivation, Red – after photoactivation). Line - normalized double-gaussian-fitted population averages (**B**) Orientation preference visually responsive neurons before and after photoactivation. (**C**) Orientation selectivity before and after photoactivation. (Error bars represent SEM in all data panels).

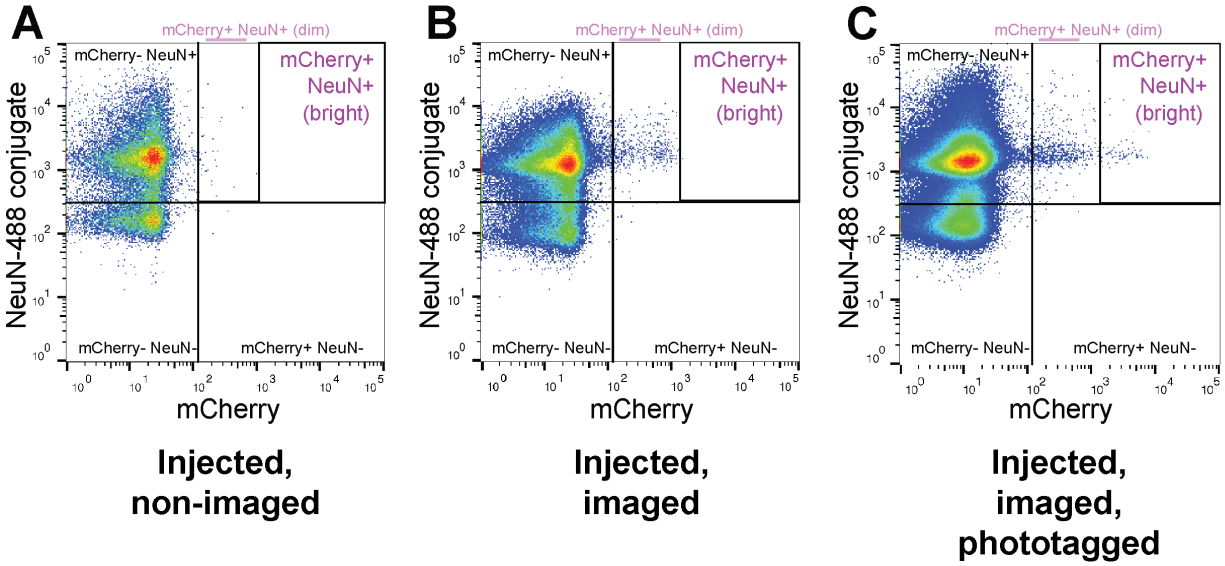

Figure S7. FACS Gating based on mCherry fluorescence. (**A**) representative FACS graph for samples that were injected but not imaged. (**B**) samples that were injected and imaged. (**C**) samples that were injected, imaged, and phototagged.

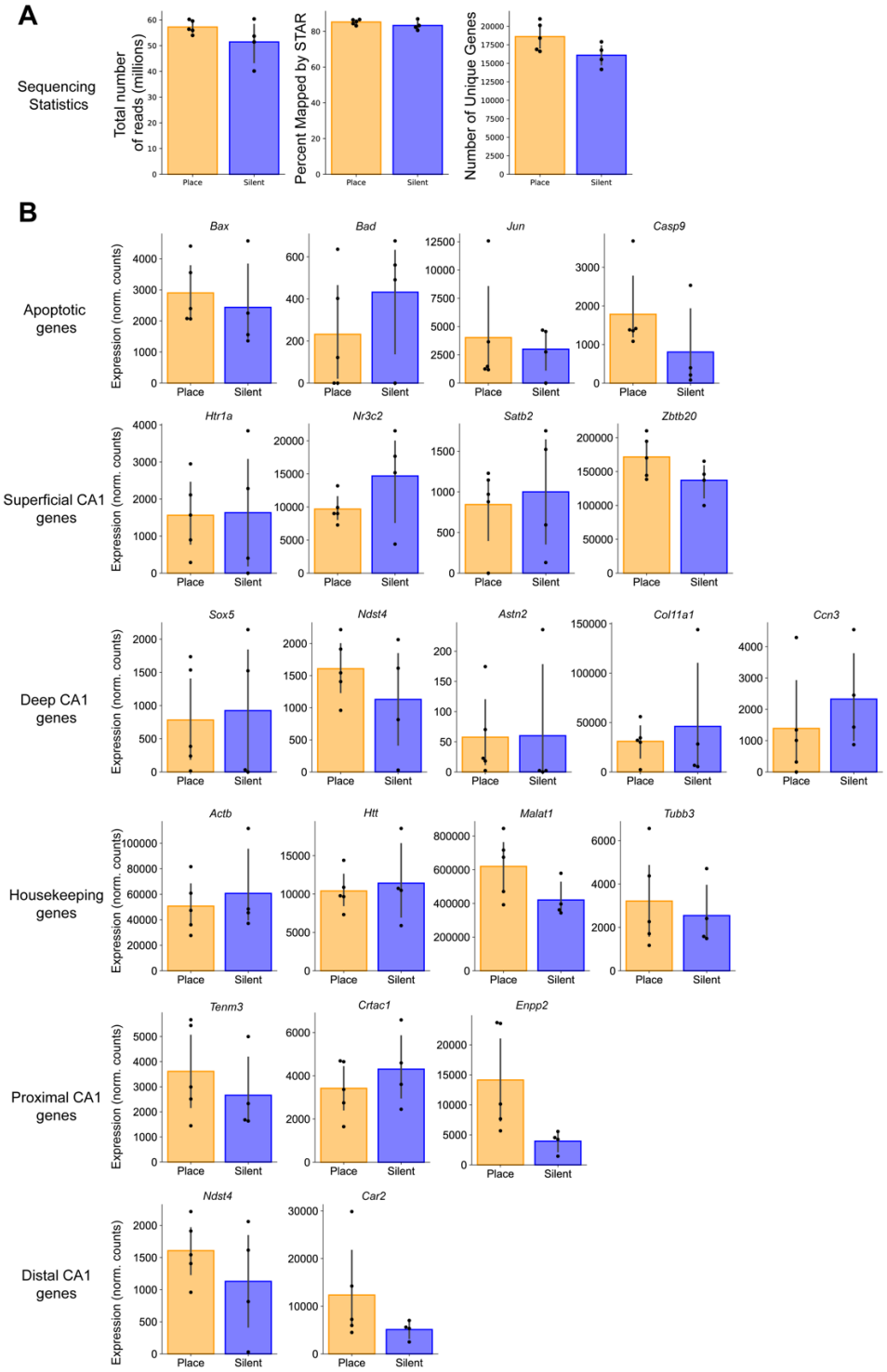

Figure S8. Additional data on transcriptomics analysis of place and silent cells. (**A**) Sequencing statistics for all 'place' and 'silent' cell samples. Total number of reads - 40 to 60 million reads, 54.64 ± 2.09, n = 9. Percent mapped by STAR - 80.58 to 86.92%. 84.33 ± 0.73. Number of unique genes - 14176 to 20990, 17486 ± 714. (**B**) Normalized counts for groups of genes plotted for 'place' versus 'silent'. Here we show that gene expression of apoptotic genes, superficial CA1 genes, deep CA1 genes, housekeeping genes, proximal CA1 genes, and distal CA1 genes are not different between the two groups (FDR adjusted p-value. *<0.05, **<0.001, ***<0.001, PyDeSeq2. All comparisons in this figure are not significant).

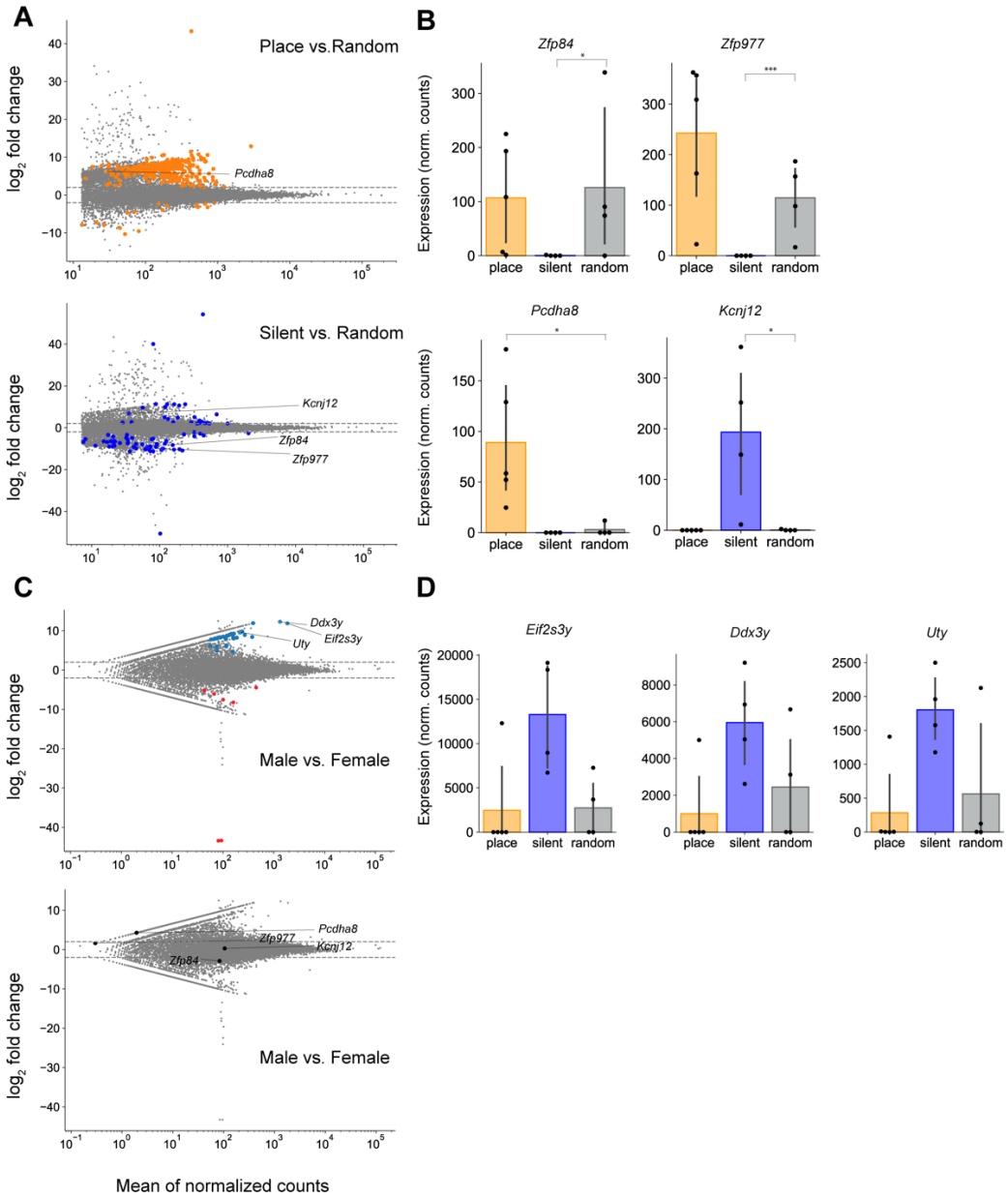

Figure S9. Additional data on transcriptomics analysis of place and silent cells. (**A**) Top: MA plot of 'place' versus 'random'. Differentially expressed genes (DEGs) are labeled in orange. Bottom: MA plot of 'silent' versus 'random'. DEGs are labeled in blue. Both: DEGs that are common for 'place' versus 'random' were highlighted and labeled. (**B**) Normalized counts for 4 example genes that are significantly differentially expressed across comparisons (FDR adjusted p-value. *<0.05, **<0.001, ***<0.001, PyDeSeq2. Showing here a comparison of 'place' versus 'random' or 'silent' versus 'random'. 'Place' versus 'silent' comparisons were shown in Figure 3). (**C**) MA plot of male versus female for the 'random' dataset. Top: Y-linked genes that are differentially expressed between sex are highlighted and labeled. Bottom: same four genes in panel A and B are highlighted and labeled. They are not differentially expressed between sex (FDR adjusted p-value. *<0.05, **<0.001, ***<0.001, PyDeSeq2. Otherwise, comparisons are not significant). (**D**) Normalized counts for 3 example DEGs between male and female.

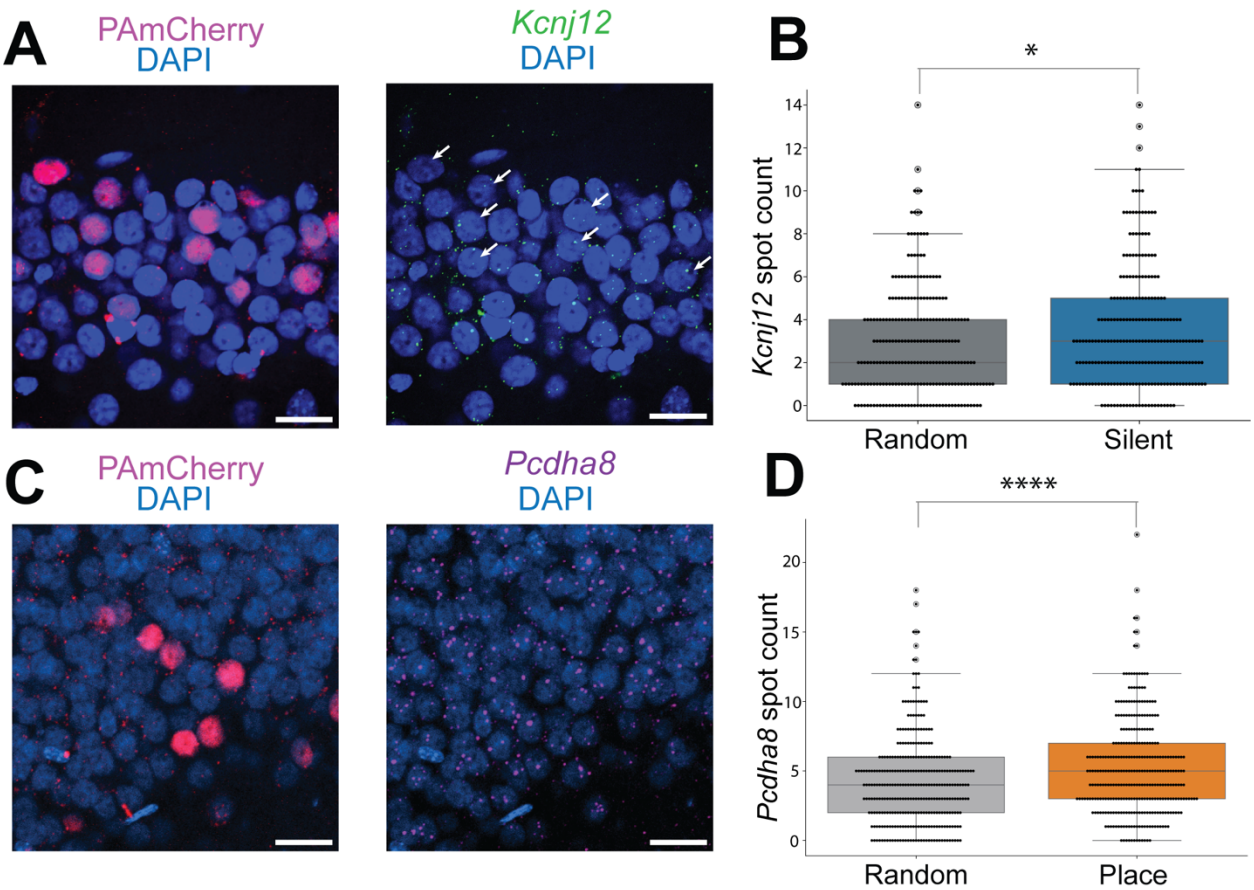

Figure S10. Spatial distribution of selected gene transcripts. (**A**) Left: Confocal horizontal image showing tagged silent cells expressing PAmCherry (red with nuclei counterstained by DAPI (blue). Scale bar: 20 µm. Right: Confocal image of the same tagged tissues as in (A), hybridized with a probe for *Kcnj12* transcripts (green) using RNAscope Multiplex Assay v2. Nuclei are counterstained with DAPI (blue). Scale bar: 20 µm. For images shown in A&B, red mCherry image was obtained at 20x zoom pre-RNAScope; blue DAPI channel and green Kcnj12 channels were obtained at 20x zoom post RNAScope. (**B**) Box plot comparing the expression levels of *Kcnj12* in tagged cells (n=247, n=3 mice, median=3, IQR=4) and randomly selected non-tagged cells (n=247, n=3 mice, median=2, IQR=3). Mann-Whitney U Test, p-value = 3.16e-2). **(C)** Left: Confocal horizontal image showing tagged place cells expressing PAmCherry (red with nuclei counterstained by DAPI (blue). Scale bar: 20 µm. Right: Confocal image of the same tagged tissues as in (A), hybridized with a probe for Pcdha8 transcripts (magenta) using RNAscope Multiplex Assay v2. Nuclei are counterstained with DAPI (blue). Scale bar: 20 µm. (D) Box plot comparing the expression levels of *Pcdha8* in tagged cells (n=321, n=3 mice, median=5, IQR=4) and randomly selected non-tagged cells (n=321, n=3 mice, median=4, IQR=4). Mann-Whitney U Test, p-value = 1.58e-4). Boxplots show the 25th, 50th (median), and 75th quartile ranges, with the whiskers extending to 1.5 interquartile ranges below or above the 25th or 75th quartiles, respectively. Outliers are defined as values extending beyond the whisker ranges.

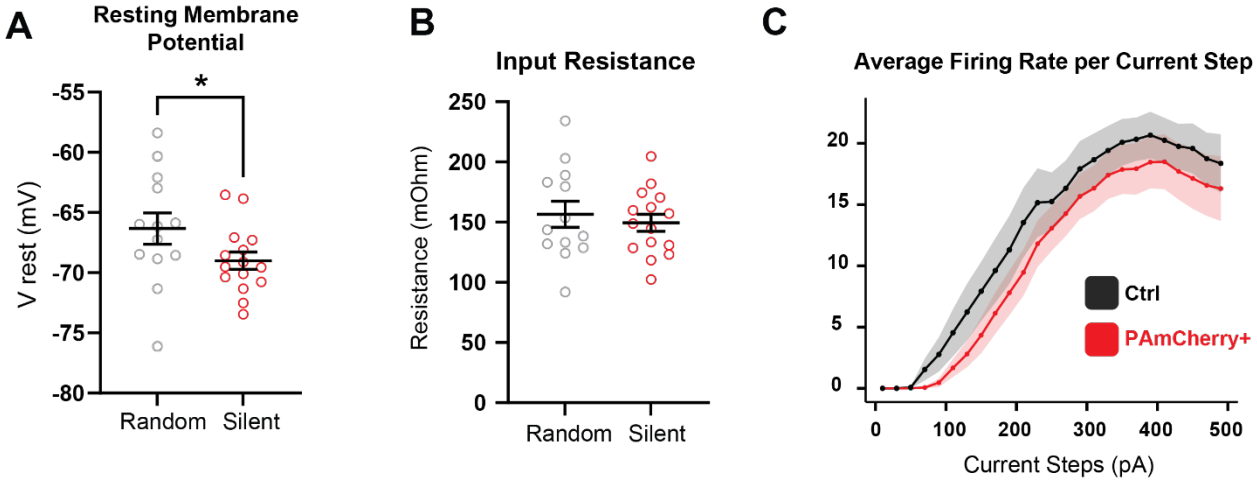

Figure S11. Silent cells display a decrease in resting membrane potential. (**A,B**) Quantified data of Resting membrane potential and Input resistance in Random (non-silent, *Ctrl*) and silent (PAmCherry+) CA1 PNs (Random n = 19 cells from 4 mice; Silent n = 12 cells from 4 mice). (Mann-Whitney U test. Resting Membrane Potential: p-value=0.0401; Input Resistance: p-value=0.6832; * $p<0.05$). (**C**) Average firing rate per current step in each condition. (Error bars represent SEM in all data panels).

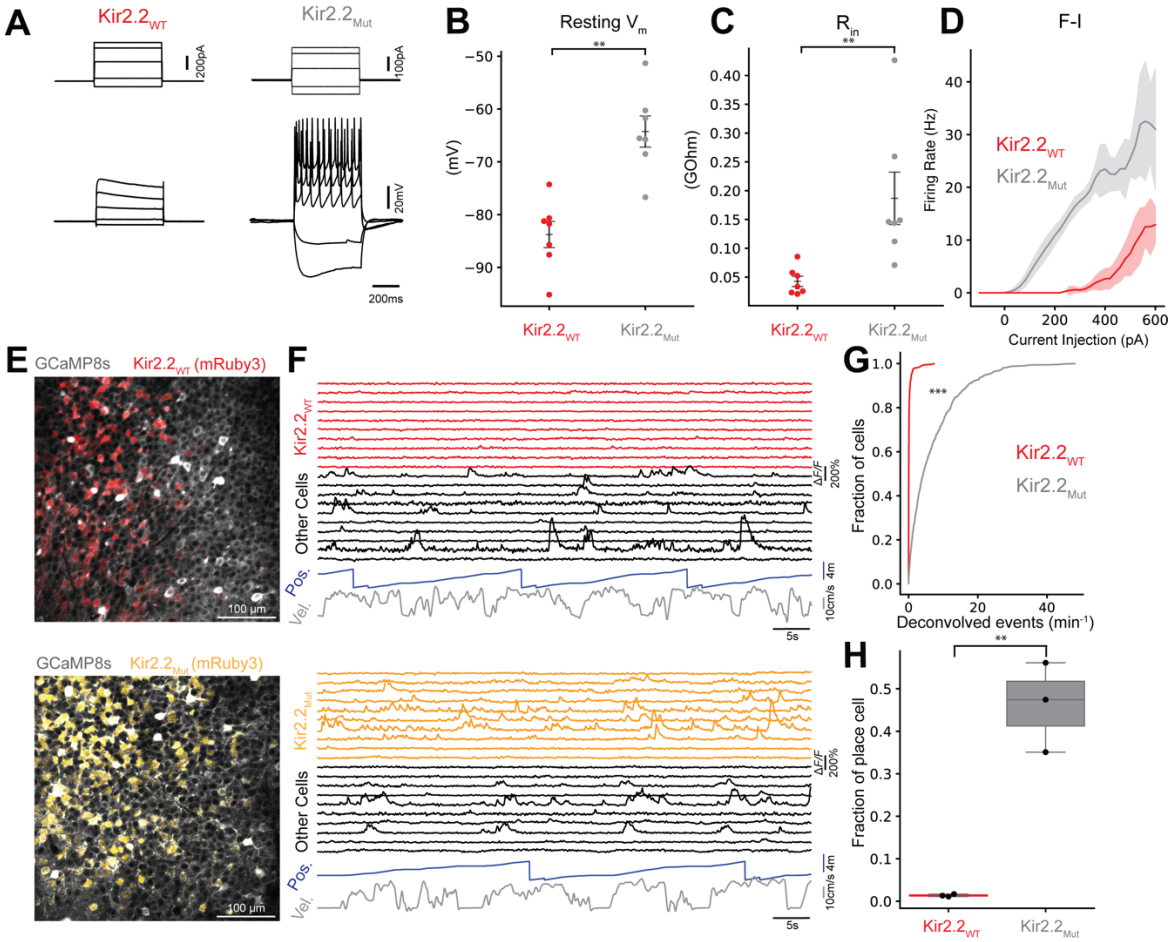

Figure S12. Ectopic expression of Kir2.2 silences CA1 neurons and reduces place cell percentage. (**A**) Representative traces of current (top) and voltage (bottom) as recorded in current clamp mode from cells that express either Kir2.2$_{WT}$ or Kir2.2$_{Mut}$. Cells that express Kir2.2$_{WT}$ shows less action potentials despite higher current injections (current scale bar left: 200pA, right: 100pA). (**B,C**) Quantified data of resting membrane potential (**B**) and input resistance (**C**) in Kir2.2$_{WT}$ and Kir2.2$_{Mut}$ cells (Kir2.2$_{WT}$ n = 7 cells from 2 mice; Kir2.2$_{Mut}$ n = 7 cells from 2 mice). (Mann-Whitney U test. Resting Membrane Potential: p-value=0.001; Input Resistance: p-value=0.001). (**D**) Average firing rate per current step in each condition. (**E**) Representative 2P imaging field of view (FOV) of GCaMP and Kir2.2 channels in the CA1 pyramidal layer. Top: mouse is injected with AAV-hSyn-GCaMP8s, AAV-hSyn-FLEX-Kir2.2$_{WT}$-mRuby3 and AAV-hSyn-Cre to express GCaMP and sparse expression of Kir2.2$_{WT}$. Gray: GCaMP; Red: Kir2.2$_{WT}$. Bottom: mouse is injected with AAV-hSyn-GCaMP8s, AAV-hSyn-FLEX-Kir2.2$_{Mut}$-mRuby3 and AAV-hSyn-Cre to express GCaMP and sparse expression of Kir2.2$_{Mut}$ as a control against Kir2.2$_{WT}$. Gray: GCaMP; Orange: Kir2.2$_{Mut}$.Scale bars: 100 mm. (**F**) Representative traces of dF/F, position and velocity of 2P recording during spatial navigation. For both top and bottom plots: top 10 traces are from cells that are infected with either Kir2.2$_{WT}$ or Kir2.2$_{Mut}$, bottom 10 traces are from cells in the same recording field of view but are not infected with either Kir2.2 AAVs. Note for overexpression of Kir2.2$_{WT}$, other cells in the recording FOV are not affected by the channel overexpression and still exhibit normal calcium transients, and Kir2.2$_{Mut}$ control cells still show normal activity. (**G**) Deconvolved events per minute from all cells across all mice that are infected with either Kir2.2 AAVs (n = 345 Kir2.2$_{WT}$ cells from 3 mice, n = 620 Kir2.2$_{Mut}$ cells from 3 mice, Mann-Whitney U Test, p-value = 1.74e-119). (**H**) Fraction of place cells in all cells from all mice that are infected with either Kir2.2 AAVs (Kir2.2$_{WT}$ mean = 0.013, IQR = 0.003. Kir2.2$_{Mut}$ mean = 0.462, IQR = 0.105. Unpaired t-test, p-value = 0.018). (Error bars represent SEM in all data panels).

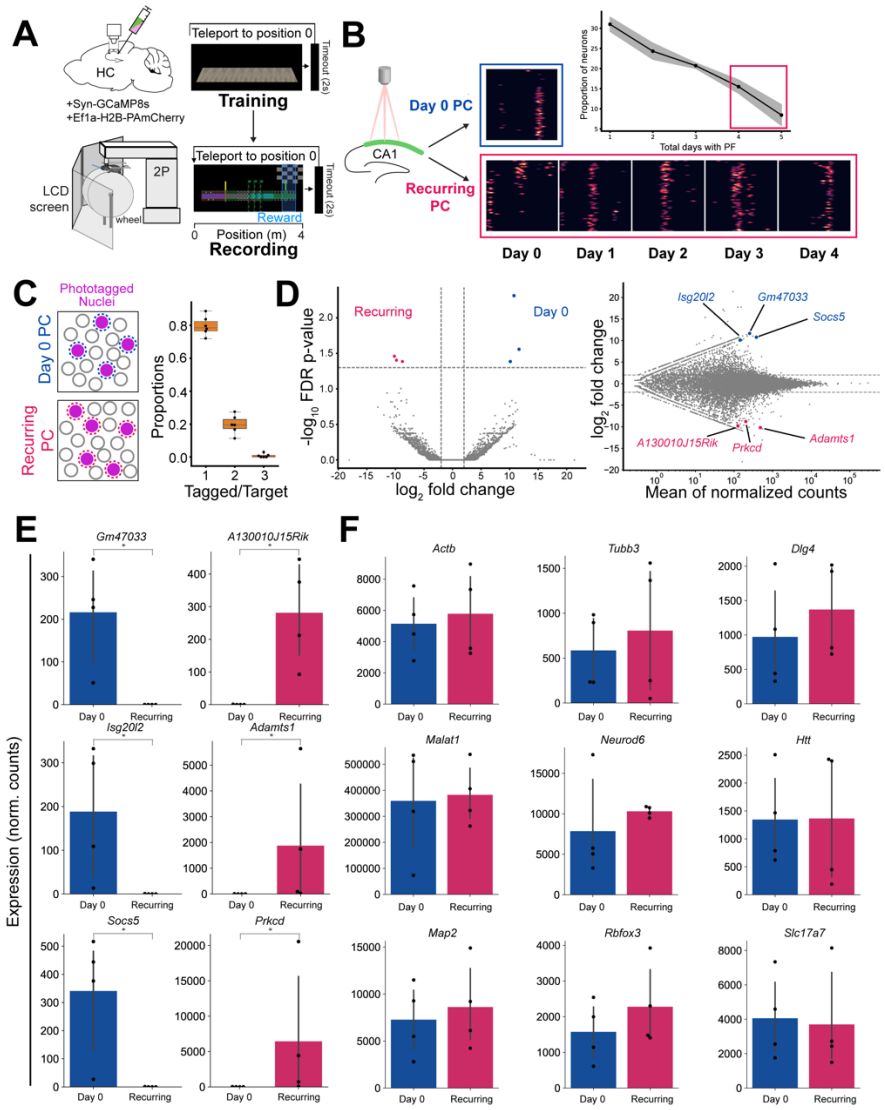

Figure S13. Transcriptional profiling of Day 0 and Recurring place cells. (**A**) Schematics of imaging and behavior setup. Mice were trained in featureless environments and recorded in a feature-rich environment. (**B**) Heatmaps of normalized ΔF/F activity from one sample day 0 place cell and one sample recurring place cell over 60 laps during VR navigation for either one day or across five days of recording. Upper right: quantification of proportion of neurons with respective numbers of place fields across 5 recording days (solid line: mean, shaded area: mean + s.e.m, n = 4 mice). (**C**) Left: schematics of *in vivo* photoactivated nuclei. 'Day 0' place cell sample and 'Recurring' place cell samples from different mice were collected for FACS and Meso-seq. Right: Proportion of single, double, and triple-tagged nuclei following phototagging of a single place cell. (**D**) Left: volcano plot of Meso-seq differential expressed gene (DEG) analysis for 'Day0' and 'Recurring' place cells. Right: Meso-seq MA plot depicting DeSeq2 normalized gene counts versus log2 fold change of Day 0/Recurring place cells samples. Day 0 and Recurring place cells are similar in genetic profiles with only 6 differentially expressed genes identified. Genes that are significantly different are labeled in blue and magenta (same as above). Genes shown in panels *E* are highlighted and labeled in *D*. (significantly different genes are shown in blue and magenta. blue: enriched in 'Day 0' cells; magenta: enriched in 'Recurring' cells). (**E**) Bar graph showing the normalized counts for differentially expressed genes (FDR adjusted p-value. *<0.05, **<0.01, ***<0.001, PyDeSeq2. Otherwise, comparisons are not significant). (**F**) Bar graph showing the normalized counts for genes that are not differentially expressed. Boxplots show the 25th, 50th (median), and 75th quartile ranges, with the whiskers extending to 1.5 interquartile ranges below or above the 25th or 75th quartiles, respectively. Outliers are defined as values extending beyond the whisker ranges.

Table 1

Mouse	Sex	Group	Place #	Silent #	Active Non-Place #	Mask #	Tag #
12-10	Male	Place	119	208	1754	119	112
12-20	Female	Place	250	470	1232	218	168
12-21	Female	Place	89	1040	701	74	73
12-27	Female	Place	132	547	548	119	119
12-37	Female	Place	126	290	1440	119	115
12-9	Male	Silent	9	152	655	152	87
12-12	Male	Silent	28	230	287	230	89
12-31	Male	Silent	129	305	1238	200	97
12-34	Male	Silent	187	303	571	113	79

Supplementary Movie 1. Phototagging
Real-time movie of *in vivo* two-photon imaging and phototagging of neurons. Imaging was performed at 1040 nm to visualize change in PAmCherry fluorescence. During phototagging, the 810-nm laser was scanned over target nuclei and the PMT was blanked. A frame average of 64 frames was applied for resolution and clarity. Final video was edited to include scale bar and laser switches. Video time is not representative of actual recording time.

Supplementary Movie 2. Registered *in vivo* and *ex vivo* image stacks
Three-dimensional rendering of registered z-stacks of *in vivo* and *ex vivo* tissue volume of the CA1 pyramidal layer with phototagged nuclei. Corresponding to *Figure 1F* and *Figure S1C,D*. Magenta: PAmCherry *in vivo* (captured on Bruker 2P microscope, wavelength = 1070 nm). Orange: PAmCherry *ex vivo* (captured on A1 HD25, Nikon Instruments Inc., wavelength = 568 nm)

Supplementary Table 1. List of DEGs between place and silent cells
List of DEGs between place and silent cells showing log 2-fold change, mean of normalized count (baseMean), and FDR adjusted p-value. All genes in the table have an FDR-adjusted p-value less than 0.05 when comparing silent versus place cells. log2FoldChange is computed for silent versus place (positive: enriched in silent cells, negative: enriched in place cells).
File: Supplementary_Table.